Computational Materials Science 226 (2023) 112224

Contents lists available at ScienceDirect

Computational Materials Science

journal homepage: www.elsevier.com/locate/commatsci

Full length article

Phase separation kinetics of block copolymer melts confined under moving parallel walls: A DPD study

Ashish Kumar Singh, Awaneesh Singh *

Department of Physics, Indian Institute of Technology (BHU), Varanasi, 221005, Uttar Pradesh, India

ARTICLE INFO

Keywords:
DPD simulation
Phase separation
BCP melt
Lamellar morphology
Shear thinning

ABSTRACT

We use dissipative particle dynamics (DPD) simulations to study the effect of shear on domain morphology and kinetics of microphase separating critical diblock copolymer (BCP) bulk melts. The melt is confined within two parallel amorphous solid walls at the top and bottom of the simulation box. The shear is induced by allowing the walls to move in a direction with a specific velocity. We explore the following cases: (i) walls are fixed, (ii) only the top wall moves, (iii) both walls move in the same direction, and (iv) both walls move in opposite directions. After the temperature quench from an uniformly mixed state, we monitor the effect of shear on evolution morphology, scaling behavior, characteristic length scale and growth laws of the evolving system. The characteristic length scale follows typical power-law behavior at early times and saturates at late times when both walls are fixed. The length scale changes significantly with shear rates caused by wall velocities. The usual lamellar morphology, which is not achieved for case 1 within the considered simulation time steps, is noticed much earlier for the nonzero wall velocity cases. Specifically, it is seen much before in case 4 than in the other cases. We find that the shear viscosity decreases (shear-thinning) with shear rate for all the cases at a given coarsening time. Overall, we report the influence rule of shear rates on microphase separation kinetics of BCP melts. This study can provide a scheme to anticipate and design anisotropic microstructures under the application of externally controlled wall shear that may further guide in producing the various composite materials with superior mechanical and physical properties.

1. Introduction

Microphase separation of block copolymer (BCP) melts [1–5] has continued to be an active area of research for decades [6–10]. BCP is a long linear chain molecule (A_nB_m) composed of two covalently bonded incompatible sub-chains of n A- and m B-monomer beads. When a homogeneous BCP melt in its high-temperature homogeneously mixed stable phase is quenched below the critical temperature, the system becomes thermodynamically unstable. The small fluctuations in the density field grow, and the phase separation occurs, forming A-rich and B-rich phases [11–13]. Since the chemically bonded immiscible sequences cannot be separated indefinitely, their sub-chain lengths control the spatial scale. Thus, coarsening gives rise to morphologies at a microscopic length scale, i.e., micro-domains rich in either of the two components are formed. Different morphologies like lamellae, gyroids, cylinders, and spheres depend on the relative compositions (n : m) of sub-chains [1–4].

Domain coarsening is a well-known scaling phenomenon where the characteristic length scale, $R(t)$ follows a power-law equation, $R(t) \sim t^{\phi}$ asymptotically [11–13]. Here, ϕ is the growth exponent, which depends on the relevant coarsening mechanism [12]. BCP melts coarsen into the well-ordered structures differently than macrophase separation of polymer blends [14–17]. Numerous theoretical [1–4] and simulation [6,18] efforts have demonstrated that the variation of characteristic length scale with time initially follows a power-law with $\phi \sim 1/4$ in the weak-segregation regime [1] and $\phi \sim 1/3$ in the strong-segregation regime [2,3,6,18]. The segregating BCP melts evolve into frozen microstructures with various morphologies in the asymptotic limit. It is further demonstrated that the effects of hydrodynamics only accelerate the growth kinetics at pre-asymptotic stages compared to diffusive dynamics [19–23]. Similar frozen morphologies are observed at late times, as in the diffusive case [19–23].

The self-assembled BCP morphologies are the topic of vital interest due to their rapidly increasing applications in various fields such as advanced materials [24], lithography [24–26], drug delivery [24,27,28], and porous materials [24,29]. The latest applications of BCPs come from their self-assembly on the nanoscale [30]; these properties rely on the long-range order of BCP melts [31,32]. The change in morphology considerably affects the final properties of multiphase materials.

* Corresponding author.
E-mail address: awaneesh.phy@iitbhu.ac.in (A. Singh).

https://doi.org/10.1016/j.commatsci.2023.112224
Received 5 October 2022; Received in revised form 15 April 2023; Accepted 18 April 2023
Available online 28 April 2023

Therefore, coarsening domain morphology can significantly influence the final material properties.

The control over evolved morphology at the molecular scale can help develop new and robust materials with great industrial applications. Various methods such as shear [33], electric field [34], chemically patterned substrate [35], etc., have been proposed in the recent past to speed up BCP melts' segregation. Using either steady or oscillatory shear [36] is the more straightforward approach. Their application to BCPs plays a dominant role in determining their self-assembled structure. Using these methods, spherical, cylindrical, and lamellar morphologies have been illustrated successfully [37–42]. Some recent works on BCP thin films [43,44] have improved the alignment of cylindrical and spherical domain evolution using shear; it is believed that microphases try to minimize the effect of shear by reorienting themselves towards shear flow [36]. Nevertheless, most of these studies were focused mainly on either $2d$ surfaces [33,36] such as thin substrates/films [43,44] or studying the equilibrium/steady state properties [45,46] in BCP melts for a small system sizes [37–42]. Thus, a detailed DPD simulation study of the kinetics of microphase separation of BCP bulk melts under the influence of shear is still lacking. In contrast to any coarse-grained models, which use uncontrolled approximations to model the velocity field, the DPD approach has the considerable advantage of naturally incorporating flow fields and the hydrodynamic effects in the system [6]. Furthermore, the influence of physical boundary and the competition between shear and phase separation kinetics in BCP melts are crucial in understanding the morphology and related properties changes [36].

Thus, a more detailed study on growth kinetics, particularly the growth exponent, scaling properties, and structural anisotropy due to variation in shear rate, are of paramount importance for a BCP melt under confinement. The shear is introduced by moving parallel walls confining the system from the top and the bottom. Herein, we choose a symmetric BCP melt where each chain has two incompatible sub-chains of equal length. The amorphous walls have the same interaction with each sub-chain; thus, both phases experience an equal amount of shear caused by the wall velocity in a particular direction. Therefore, it is natural to inquire about the shear effect on the microphase separation kinetics in BCP melts. We ask the following questions: does shear stimulate or delay the segregation process in the bulk system? Further, do microscale morphologies vary with low and high shear rates? Finally, what would be the effect on scaling functions and growth laws?

The shear generated for various scenarios is analyzed using the DPD simulation technique. However, experimental replication of some cases can be difficult. For instance, case 3, where both walls move in the x-direction, appears particularly difficult to realize experimentally. In contrast, inducing shear by moving either the top or bottom wall in case 2 may be achievable through various experimental methods. These include fabricating flat-sheet membranes [43,44], polymer membrane casting [47], flow-induced crystallization [48], nano-structuring in gelled emulsions [49,50] and bulk BCP melts [51]. It is worth noting that we found no experimental evidence of case 3 to the best of our knowledge. Nonetheless, this simulation study can provide valuable insights into work that may be challenging to conduct in theory or experiments. Considering the limitations and fea-sibility of experimental approaches in studying complex systems is essential, and simulation techniques can help bridge the gap between theory and experiments. Additionally, future re-search may focus on developing new experimental methods to replicate these challenging scenarios and validate simulation findings.

In the next section, we briefly describe the DPD methodology that captures the effect of shear on the phase separation kinetics of BCP melts. Then, the simulation results are discussed in Section 3. Finally, we conclude the paper in Section 4.

2. Methodology

2.1. Dissipative particle dynamics

DPD is a powerful simulation technique to study the kinetic behavior of complex soft mesoscale systems [16,52–54]. In DPD, a cluster of particles or molecules is modeled as a single bead, which makes DPD a more thriving numerical tool to simulate the system over a higher length and time scale than a traditional molecular dynamics (MD) simulation technique [55–57]. We integrate Newton's equation of motion for the system's time evolution:

$$\frac{d\vec{p}_i}{dt} = \vec{f}_i(t) = \sum_{i \neq j} \vec{F}_{ij} \tag{1}$$

where $\vec{p}_i = m_i \vec{v}_i$, $\vec{v}_i = d\vec{r}_i/dt$, and $\vec{r}_i$ denote the momentum, velocity, and position vectors of ith bead. The force $\vec{f}_i(t)$ on ith particle by all other j particles consist of three pairwise additive components: (i) $\vec{F}^C_{ij}$ represents the conservative force, (ii) $\vec{F}^D_{ij}$ denotes the dissipative force, and (iii) $\vec{F}^R_{ij}$ imply the random force such that $\vec{F}_{ij} = \vec{F}^C_{ij} + \vec{F}^D_{ij} + \vec{F}^R_{ij}$.

The conservative force describes the pairwise interaction between the beads. The most common and simple choice for $\vec{F}^C_{ij}$ is [52]

$$\vec{F}^C_{ij} = \begin{cases} a_{ij}\left(1 - r_{ij}/r_c\right)\hat{r}_{ij}, & r_{ij} < r_c \\ 0, & r_{ij} \geq r_c \end{cases} \tag{2}$$

which is a linear soft repulsive interaction up to a cut-off distance r_c. Here, a_{ij} denotes the maximum repulsion of the conservative force, $\vec{r}_{ij} = \vec{r}_j - \vec{r}_i$, $r_{ij} = |\vec{r}_{ij}|$ and $\hat{r}_{ij} = \vec{r}_{ij}/r_{ij}$. The dissipative force $\vec{F}^D_{ij}$ has the following mathematical form

$$\vec{F}^D_{ij} = -\gamma \omega_D(r_{ij})(\hat{r}_{ij} \cdot \vec{v}_{ij})\hat{r}_{ij} \tag{3}$$

where γ is the friction coefficient or strength of viscus dissipation, $\omega_D(r_{ij})$ is the weight function of the dissipative force, and $\vec{v}_{ij} = \vec{v}_i - \vec{v}_j$. The effect of thermal fluctuation is described by [52]

$$\vec{F}^R_{ij} = \sigma \omega_R(r_{ij}) \Delta t^{-1/2} \xi_{ij} \hat{r}_{ij} \tag{4}$$

where σ is the strength of the random force, $\omega_R(r_{ij})$ is the corresponding weight function, and ξ_{ij} denotes the Gaussian random variable with zero mean $\langle \xi_{ij}(t) \rangle = 0$ and unit variance $\langle \xi_{ij}(t)\xi_{kl}(t') \rangle = (\delta_{ik}\delta_{jl} + \delta_{il}\delta_{jk})\delta(t - t')$ [52,53]. The symmetry relations $\vec{F}_{ij} = -\vec{F}_{ji}$, $\xi_{ij} = \xi_{ji}$, and the force $\vec{F}^D_{ij}$ and $\vec{F}^R_{ij}$ act along the line joining bead centres ensure the momentum conservation [52,53].

To attain the correct canonical thermodynamic equilibrium state of a system at a temperature T, the strength of the random (σ) and dissipative (γ) forces must follow the fluctuation–dissipation relation [53,54] $\sigma^2 = 2\gamma k_B T$ where k_B is the Boltzmann constant; their corresponding weight functions must be coupled as $\omega_D(r_{ij}) = \left[\omega_R(r_{ij})\right]^2$. The common choice for the weight function [52] is $\omega_D(r_{ij}) = \left(1 - r_{ij}/r_c\right)^2$ for $r_{ij} < r_c$. However, we can choose other forms of weight functions given that the above two conditions are satisfied.

2.2. Model parameters and other details

The system evolution is followed by integrating the equations of motion shown in Eq. (1) using a modified velocity-verlet algorithm [58]. In DPD simulations, cut-off radius r_c is commonly considered as a characteristic length scale, and $k_B T$ as a characteristic energy scale [52]. Each DPD bead is considered to have equal mass $m_i = m$. The total number density of beads is set to $\rho = 3$ appropriate for the DPD simulation of liquids; this choice of ρ also ensures that the system is far away from the gas-liquid transition [52,53]. The simulation results are presented in reduced DPD units with the parameters r_c, m, and $k_B T$, all set to 1.0 [52]. Following the dimensional analysis, the characteristic time scale is defined as $\tau = \left(m r_c^2/k_B T\right)^{1/2}$, which gives $\tau = 1.0$ in reduced DPD units. The time scale obtained by

using the conventional DPD procedure yields $\tau = 8.3$ ps, which is known as the intrinsic time scale for producing accelerated dynamics due to softcore potential [52,59,60]. However, to get a more relevant time scale, we can correlate the collective diffusion coefficient of the polymeric melt in the DPD simulations, $D_{sim} \approx 1.74 \times 10^{-2}$ nm$^2/\tau$, to the experimental time scales $D_{exp} \approx 2.00 \times 10^{-11}$ m^2/s [61]. Thus, the estimated characteristic time scale for our simulation is $\tau \approx 0.87$ ns. We chose the integration time step $\Delta t = 0.02$ [17]. The dissipation parameter in Eq. (4) is set to $\gamma = 4.5$, which is suitable for the system to reach the equilibrium temperature more rapidly and provide numerical stability for the specific time steps [52].

We set the value of repulsive interaction strength $a_{ij} = 25$ for the interaction between chemically compatible BCP beads (*i.e.*, $a_{AA} = a_{BB} = 25$). This choice is made to reproduce the compressibility of water by coarse-graining ten water molecules into one bead [52–55]. Therefore, the characteristic length in the actual units are estimated to be $r_c = 0.97$ nm [16,17]. The interaction parameter, $a_{ij} = 60$ for chemically incompatible beads (*i.e.*, $a_{AB} = 60$). The interaction of A and B beads with the wall beads is set to $a_{ij} = 45$. In our DPD simulation, we quench the system at reduced temperature $T = 1$, which we see in a short while that the chosen temperature is well below the critical temperature for the corresponding phase separation to take place [16,17].

We simulate BCP chains as bead–spring model where the beads of each sub-chains are connected by harmonic bond potential [60,62], $E_b = \frac{k_b}{2}(r - r_0)^2$ where $k_b = 128$ is the elastic constant, and $r_0 = 0.5$ is the equilibrium bond length [16,57]. The stiffness of the polymer chain is handled by the angle potential, $E_a = \frac{k_a}{2}(\cos\theta - \cos\theta_0)^2$, where $k_a = 5$ is the strength of the angle potential. The angle between two successive bonds along the chain is θ. We have taken the equilibrium value $\theta_0 = 180$ [56–58,60,62]. Since DPD utilizes softcore interaction potential between the beads, there could be an unphysical bond crossing between the BCP chains. To mitigate that, we used *modified segmental repulsion potential* (mSRP) [63]. In this formulation, pseudo beads are considered at the center of all bonds. These beads interact with a softcore repulsive interaction [63], $\vec{F}_{ij}^{mS} = k_{mS}\left(1 - r_{ij}/r_c^{mS}\right)\hat{r}_{ij}$, for $r_{ij} < r_c^{mS}$ where $k_{mS} = 100$ (in reduced DPD units) is the force constant. The cutoff distance for the mSRP interaction is taken as $r_c^{mS} = 0.6$. We use the LAMMPS simulation package [58] with mSRP code [63] to integrate the equations of motion.

The box size used in our DPD simulation is $L_x \times L_y \times L_z = 64 \times 64 \times 64$; thus, the total number of DPD beads in the simulation box is $N = \rho \times L^3 = 7,86,432$. We consider a critical BCP melt ($n : m = 1 : 1$) with chain length $N_p = 32$ (degree of polymerization). Total number of A- and B-type beads is $N_A = N_B = 3,80,928$ ($\phi_A = \phi_B = 4.843 \times 10^{-1}$), *i.e.*, $\rho_A = \rho_B = 1.453$. The total number of BCP chains in the simulation box is $N_{BCP} = 23{,}808$. The period boundary conditions are applied in x- and y- directions, whereas both walls bound the simulation box in the transverse z-direction. The height of each wall is set to $h = 1.0$. The walls are also made of DPD beads in an amorphous arrangement with a number density $\rho_w = 3$; therefore, the total number of wall beads is $N_w = 24{,}576$, so the volume fraction is $\phi_w = 3.125 \times 10^{-2}$.

When walls are fixed, corresponding velocity components v_{wx}, v_{wy}, and v_{wz} are set to zero (case 1). To shear the system, we let the walls move in x-direction with a constant velocity, $\vec{v}_w \in (v_{wx}, v_{wy} = 0, v_{wz} = 0)$. We consider three cases depending on the direction of the wall's motion: (i) top wall moves in the positive x-direction (case 2) with $v_{wx} = 0.1$, 0.5, and 1.0, while the bottom wall is fixed. (ii) The top and the bottom walls move in the same direction (case 3) with the same wall velocities as in case 2. (iii) Both walls move in the opposite directions, the top wall moves in the positive x-direction, and bottom wall in the negative x-direction; we set this condition as case 4. The bounce-back boundary condition is applied at the wall–fluid interfaces [64] to prevent the BCP beads from penetrating the amorphous walls and to produce no-slip boundary conditions with minimal interfacial density oscillation [65,66]. Therefore, the shear rate ($\dot{\gamma}$) applied to the system takes the values $\dot{\gamma} = 1.56\times10^{-3}, 7.80\times10^{-3}$, and 1.56×10^{-2} corresponding to the wall velocities $v_{wx} = 0.1, 0.5$, and 1.0, respectively, in the dimensionless DPD units. Thus, the applied shear rate in our simulation ranges from $\dot{\gamma} = 1.8 \times 10^5$/s to 1.8×10^6/s, which are within the same order of magnitude as those used in high shear rate experiments in microfluidic devices [67,68].

To demonstrate the effect of shear, we compute shear viscosity, η using the technique developed by Muller-Plathe [69,70]. In this technique, momentum flux is imposed on the system by the exchange of momentum of atoms along a particular direction (say z-direction). The average velocity profile is generated as a response to momentum flux. Shear viscosity can be calculated from the slope of velocity profile and imposed momentum flux using the equation: $j_z(p_x) = -\eta\left(\partial v_x/\partial z\right)$, here $j_z(p_x)$ is the momentum flux, and $\partial v_x/\partial z$ is the velocity gradient or shear rate. Further, we quantitatively evaluate the anisotropic degree of evolved morphology by calculating the anisotropy parameter $D_{xy}(t)$ as [71,72];

$$D_{xy}(t) = \frac{\sum[(k_x^2 - k_y^2)/k^2]S(k_x, k_y, k_z)}{\sum S(k_x, k_y, k_z)}. \tag{5}$$

Here, k_x and k_y are the components of wave vector $\vec{k}$ in the xy-plane for a fixed k_z where $k^2 = k_x^2 + k_y^2 + k_z^2$, and $S(k_x, k_y, k_z)$ denotes the structure factor at a point (k_x, k_y, k_z) in Fourier space. Similarly, we calculate the anisotropy parameter, $D_{yz}(t)$, and $D_{xz}(t)$ in the yz and xz planes, respectively. Note that, for a perfect isotropic system, $D_{ij} \simeq 0$ and for a fully anisotropic system, $D_{ij} \to 1$.

2.3. Morphology characterization and scaling functions

The two most desirable and experimentally relevant functions to characterize the evolution morphology are the correlation function and its Fourier transform, the structure factor [12,13]. We introduce the two-point equal-time correlation function as

$$C(\vec{r}, t) = \left\langle \psi\left(\vec{r}_1, t\right)\psi\left(\vec{r}_2, t\right)\right\rangle - \left\langle \psi\left(\vec{r}_1, t\right)\right\rangle\left\langle \psi\left(\vec{r}_2, t\right)\right\rangle \tag{6}$$

where $\psi(\vec{r}, t)$ denotes the order parameter. The structure factor is defined as

$$S(\vec{k}, t) = \int d\vec{r}\exp\left(i\vec{k}\cdot\vec{r}\right)C(\vec{r}, t) \tag{7}$$

where $\vec{k}$ is the scattering wave vector.

The order parameter $\psi(\vec{r}, t)$ is obtained as the local density difference of the constituents located at $\vec{r}$ at a given time t [14,15],

$$\psi(\vec{r}, t) = \frac{n_A(\vec{r}, t) - n_B(\vec{r}, t)}{n_A(\vec{r}, t) + n_B(\vec{r}, t)} \tag{8}$$

where $n_A(\vec{r}, t)$ and $n_B(\vec{r}, t)$ represent the local number of A and B types of beads calculated as follows: we divide the simulation box into non-overlapping unit cubes and then count the number of A and B types of beads in each unit cube. Thus, from Eq. (8) $\psi(\vec{r}, t) \in (0, 1)$ for $n_A(\vec{r}, t) > n_B(\vec{r}, t)$, and $\psi(\vec{r}, t) \in (0, -1)$ for $n_A(\vec{r}, t) < n_B(\vec{r}, t)$. However, for $n_A(\vec{r}, t) = n_B(\vec{r}, t)$, we assign $\psi(\vec{r}, t) \in (0, 1)$ or $\psi(\vec{r}, t) \in (0, -1)$ with equal probability [15].

The number of peaks in the structure factor or the oscillatory behavior of the correlation function after zero-crossing signifies the periodicity of evolving morphology in the phase separating BCP melts. In our simulation, we spherically average $C(\vec{r}, t)$ and $S(\vec{k}, t)$ for better statistics. The corresponding quantities are denoted by $C(r, t)$ and $S(k, t)$, respectively. The characteristic length scale, $R(t)$ is defined as the distance over which $C(r, t)$ decays to a fraction of its maximum value ($C(r, t)|_{r=0} = 1$). There are a few other definitions of $R(t)$, but they are equivalent in the asymptotic limit; they differ only by some constant multiplicative factors in the scaling regime [73,74]. Herein, the distance over which the correlation function decays to 0.2 provides a good measure of $R(t)$ [73,75].

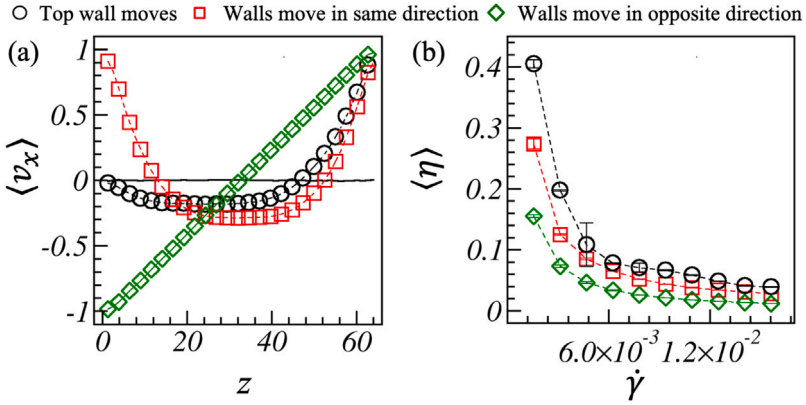

Fig. 1. (a) Average velocity profile, $\langle v_x \rangle$ is plotted along the z-direction at a higher shear rate, $\dot{\gamma} = 1.56 \times 10^{-2}$. The different symbol types at the top represent the cases studied here. (b) The variation of shear viscosity, $\langle \eta \rangle$ against $\dot{\gamma}$ at $t = 5 \times 10^3$ for all the cases denoted by the various symbol types.

The basic assumption of scaling is the existence of a unique characteristic length scale $R(t)$. The dynamical scaling form of the correlation function and the structure factor has the following form [12,13]:

$$C(r,t) = f(r/R(t)) \tag{9}$$

$$S(k,t) = R(t)^d g(kR(t)) \tag{10}$$

where $f(r/R(t))$ and $g(kR(t))$ are the corresponding scaling functions. We plot the length scale, $R(t)$ vs. t on a logarithmic scale to estimate the appropriate growth exponent ϕ [17,76–78]. Further, we follow another intuitive way to verify the same by computing the effective growth exponent as

$$\phi_{eff} = \log_\alpha \left[R(\alpha t)/R(t) \right] \tag{11}$$

and plot it against inverse of domain size $1/R(t)$ where we set the log-base $\alpha = 2$ [79]. In general, the domain growth law for any typical phase-separating system can be written as $R(t) = R_0 + at^\phi$. Here, R_0 denotes the average domain size of the transient growth regime when the system becomes unstable due to fluctuations at an early time t_0 since the quench (i.e., from $t = 0 \rightarrow t_0$). R_0 and a are temperature and composition-dependent constants [17,76–78]. The transient growth regime is usually negligible for a phase-separating system with critical compositions. However, evolution begins with more extensive transient growth regimes before the nucleation and growth set in for a system with off-critical compositions. Therefore, one can redefine the average domain size, $R(t) \equiv R(t) - R_0$, and the time $t \equiv t - t_0$ such that $R(t) \sim t^\phi$ to obtain the appropriate growth exponent, ϕ [76,78]. The values of t_0 and corresponding R_0 are provided in Table S1 (in SI) for all the cases discussed here.

3. Numerical results

In this section, we discuss the numerical results obtained for microphase separating symmetric BCP melt (A_nB_n; $n = 16$) confined within two parallel amorphous walls in the transverse z-direction. At the onset of the DPD simulation, we first equilibrate the initial system for $t = 2 \times 10^5$ at a high-temperature $T = 5$ (in reduced DPD units) to prepare a uniformly mixed (homogeneous or uncorrelated state). The shear rate is set to zero during the equilibration process. We then reset the time at $t = 0$, quench the system at a lower temperature $T = 1$, and monitor the evolution pattern at different times. We typically performed five independent simulation runs for the ensemble averaging for the scaling and growth laws. However, for the velocity profiles and viscosity calculation, averaging is done over ten ensembles.

To begin with, we first try to understand the average velocity profile of the system at different shear rates. Since wall beads are allowed to move along the x-direction with a constant velocity v_{wx}, the shear rate ($\dot{\gamma}$) applied to the system is fixed, and x-component of the velocity v_x plays a dominant role in the average velocity profile. Therefore, we generate the velocity profiles, $\langle v_x \rangle$, along the z-direction for all the cases at $\dot{\gamma} = 1.56 \times 10^{-2}$, and displayed in Fig. 1(a). For this, we divide the system into thin slabs of a unit thickness ($\Delta z = 1.0$) along the z-direction and calculate the average velocity components $\langle v_x \rangle$, $\langle v_y \rangle$, and $\langle v_z \rangle$ over all the beads in a particular slab [69,70]. The y and z components of the average velocity profile remain unaffected by the shear, so we obtain $\langle v_y \rangle = \langle v_z \rangle = 0$ for all cases (results not shown here). The solid black line in Fig. 1(a) demonstrates the velocity profile for case 1, where both walls are fixed ($\dot{\gamma} = 0.0$), and thus, $\langle v_x \rangle = 0.0$ confirms the linear momentum conservation in the system. This curve serves as a reference for the other cases studied in Fig. 1(a) at $\dot{\gamma} = 1.56 \times 10^{-2}$. In case 2 (black symbol), as the distance from the top wall increases, $\langle v_x \rangle$ gradually reduces to zero. It decreases further and attains negative values with distance, which gradually approaches zero close to the bottom wall. The velocity profile for case 3 (red curve) decreases smoothly with increasing distance from both walls and reaches a negative minimum value at $z \simeq L/2$. Finally, in case 4 (green curve), since both walls move in opposite directions, $\langle v_x \rangle$ varies linearly with distance along the z-axis, crossing zero near $z \simeq L/2$.

To understand the reason for getting negative values in velocity profile at the central region of the simulation box, we further plot $\langle v_x \rangle$ vs. z in Fig. S1(a-f) for the other cases at various parameter values. Note that wall shearing generates a flow field in the neighboring slabs of separating BCP melt. The effect of shear on successive slabs decreases with the increase of distance from the sheared wall, which eventually decays to zero at a certain distance from the wall $z \approx 48$ for case 2 in Fig. S1(a), and $z \approx 12$ and 52 for case 3 in Fig. S1(d). Following the incompressible Newtonian fluid flow conditions, the system responds to the nonequilibrium situation by inducing a momentum flow in the opposite direction to maintain momentum conservation throughout the system [69,70,80]. Recall that the linear momentum is conserved by default in DPD simulation when both walls are fixed (case 1). However, when the top wall moves (case 2), it exerts a shear stress on the BCP melt, causing its layers to slide over each other. This results in BCP melt flowing and forming layers parallel to the top wall. The layers closest to the top wall experience the highest velocity, while those near the bottom wall have the lowest velocity. It is important to note that the net flow in the system must be zero to conserve momentum [20,21,52]. Therefore, the lower flow in the bottom region must be compensated by the faster flow in the upper part of the box. As a result, there is a negative velocity profile in the central box area, where the velocity is lower than the average velocity of the BCP melt. Thus, the negative velocity profile in the central region is a consequence of the shear-induced alignment of the BCP chains, which creates a velocity gradient across the box to maintain momentum conservation. In case 3, the difference in flow velocity creates a gradient along the height of the box, with

the highest velocity near the walls in the same direction that decreases towards the center. This also leads to a negative velocity profile in the central region to maintain momentum conservation. Similarly, in case 4, the opposite wall shear generated is balanced such that the net flow in the system is zero; momentum is conserved. Consequently, a linear variation of $\langle v_x \rangle$ with distance from top to bottom, crossing zero near $z = L/2$ [69,70,80].

Furthermore, the momentum induced in the opposite direction also increases in response to the increased shear rate. Thus, we marked the enhanced negative values in the velocity profiles [69,70,80] with shear rates $\dot{\gamma} = 1.56 \times 10^{-3}$, 7.80×10^{-3}, and 1.56×10^{-2} as demonstrated in Figs. S1(a), and S1(d) with black, red, and green curves, respectively. Next, we plot $\langle v_x \rangle$ vs. z for different chain lengths of the critical BCP melt in Figs. S1(b), and S1(e) at a fixed shear rate, $\dot{\gamma} = 1.56 \times 10^{-2}$. The velocity profile values at the center become less and less negative with increasing chain length, as illustrated in black, red, and green curves for $N_p = 8, 16$, and 32, respectively. The reason could be the slower diffusive transportation of BCP chains with a high degree of polymerization as diffusion coefficient, $D \sim N_p^{-\nu}$ where $\nu = 1/2$ is the size exponent in the melt [14,81,82]. Thus, the magnitude of opposite momentum also decreases with chain length. In Fig. S1(c), and S1(f), we plot the velocity profile for different wall distance at a fixed chain length and a shear rate. Our results illustrate that the effect of equilibrium wall distance on the negative value of the velocity profile is insignificant.

The average velocity profile, $\langle v_x \rangle$ as a function of time, is plotted in Fig. S2 for all the cases mentioned at the top. First, in Fig. S2(a-c), we examined the variation of $\langle v_x \rangle$ for different shear rates mentioned in the legend for a slab of unit thickness close to the top wall. Apparently, the average velocity profile quickly saturates to a finite value as time progresses, and the magnitude of the saturation value enhances with increasing shear rates. In Fig. S2(d-f), $\langle v_x \rangle$ is plotted for different slabs along z-direction at a fixed shear rate, $\dot{\gamma} = 7.80 \times 10^{-3}$. We observed similar results as in Fig. S2(a-c); the average velocity profile as a function of time quickly saturates for all the cases as we go along the z-direction from top to bottom walls.

To understand the effect of shear on the phase separating BCP melt in bulk, we plot the variation of average shear viscosity $\langle \eta \rangle$ with $\dot{\gamma}$ in Fig. 1(b) for cases $2-4$ as denoted by the black, red, and green symbols at a late time of evolution, $t = 5 \times 10^3$. The symbol $\langle \cdots \rangle$ denotes the average over ten ensembles. For each case, the variation of $\langle \eta \rangle$ follows a similar pattern. i.e., with the increase of shear rate, a gradual decrease in viscosity is noted, illustrating the shear-thinning, which further saturates at higher shear rates ($\dot{\gamma}$). Thus confirming the smaller average domain size, $R(t)$ at higher $\dot{\gamma}$ for cases 2–4 discussed above. The shear viscosity for case 4 (green curve) is the lowest, indicating that the effect of shear is more prominent in this case than the cases 2 and 3.

In Fig. S3(a), (c), and (e), the average bond length is plotted as a function of time at different shear rates for all the cases. An enhanced bond stretching is observed on increasing shear, which is optimum for case 4 (see Fig S3(e)), where walls move in opposite directions. This bond stretching can attribute the shear thinning to the perturbation of the polymer chains under shear. However, one can also compute the normalized radius of gyration of the BCP chains in the melt for various shear rates to demonstrate the shear thinning attributed to the perturbation of the polymer chains under shear [83]. Overall, the symmetric variation of the velocity profile within positive and negative values (i.e., the momentum flow in opposite directions) ensures momentum conservation in the system. The momentum exchange further ensures the drainage of excess heat generated by friction [69]. Thus, we observe only tiny enhancements in the instantaneous temperature, $T_i \in (0.98 - 1.095)$ around the quench temperature, $T = 1.0$, but within the statistical error at various shear rates in different cases, as displayed in Fig. S3(b), (d), and (f).

3.1. Both walls are fixed

We first study case 1 with both walls fixed (no shear) to put the rest of the discussions in proper context. The evolution morphology at $t = 1.2 \times 10^2$ and $t = 5.4 \times 10^3$ are shown in Fig. 2(a); A-type beads are in red, B-type beads are in yellow, and the olive color marks the wall beads. We plot the corresponding radial distribution function (RDF), $g_{AB}(r)$ vs. radial distance, r in Fig. 2(b) at different time steps as denoted by the various symbols. The extension in peak height and the shift to higher r with time indicate the growth of A and B clusters. The black curve ($t = 1.2 \times 10^2$) shows a single lower peak at a small r, which saturates at larger r values; this demonstrates an early-time evolution of homogeneous BCP melt into tiny domains. As time progresses, $g_{AB}(r)$ begins to develop secondary peaks as displayed by the red ($t = 3.6 \times 10^2$), green ($t = 1.2 \times 10^3$), and blue ($t = 5.4 \times 10^3$) curves, respectively; this indicates the coarsening of BCPs into periodic structures. Further, the local number density profile of A-type beads, $\rho_A(y)$ along the y-direction is displayed in Fig. 2(c) for the same time sets as in Fig. 2(b). The solid black line shows the actual number density of A beads ($\rho_A = 1.453$). The increasing density profile amplitude demonstrates the growth of phase separating domains, and the oscillatory variation ascertains the periodic structure formation. The density profiles in other directions are not shown here due to brevity.

We plot the scaled correlation functions, $C(r,t)$ vs. $r/R(t)$ in Fig. 3(a) at four different times. The correlation functions at early times, $t = 1.2 \times 10^2$ (black symbol) and $t = 3.6 \times 10^2$ (red symbol), deviate from the scaling. Note that early-time domain evolution in BCP melt is analogous to spinodal decomposition in polymer blends [20]. An excellent data overlap of the correlation functions at late times, $t = 1.2 \times 10^3$ and 5.4×10^3 (denoted by the green and blue symbols), justify the dynamical scaling regimes. A more oscillatory form of $C(r,t)$ after the zero crossing characterizes the development of periodic structures in late times. The solid black line denotes the zero-crossing of $C(r,t)$. Notice that we do not observe a clear lamellar morphology within the given simulation period as displayed in Fig. 2(a) for the symmetric BCP melt with chain length $N_p = 32$ ($A_{16}B_{16}$). Since diffusion coefficient, $D \sim 1/N_p$, the formation of lamellar morphology is observed for symmetric BCP melts with shorter chains within the same simulation period, as displayed in Fig. S4(a) for $N_p = 8$ (A_4B_4) and in Fig. S4(b) for $N_p = 16$ (A_8B_8). Therefore, we need longer steps to observe lamellar morphology for BCPs with chain length $N_p = 32$. The scaled structure factor, $S(k,t)R(t)^{-3}$ vs. $kR(t)$ in Fig. 3(b) is displayed for the same times as in Fig. 3(a). As expected, we observe a crossover in the scaling functions. The structure factor data deviates at early times (indicated by the black and red symbols). Notice the narrowing peak in $S(k,t)$ and the appearance of the shoulder (at $kR(t) \simeq 4$) in the green and blue curves at $t = 1.2 \times 10^3$ and $t = 5.4 \times 10^3$; this verifies the formation of periodic morphology at the late stages of coarsening. The structure factor shows a power-law decay, $S(k,t) \sim k^{-(d+1)}$ at large wave vector ($k \to \infty$) regimes where d is the system's dimension; this is known as Porod's law [84] results from scattering off sharp interfaces.

Next, to study the domain growth law for the evolution shown in Fig. 2(a), we plot the characteristic length scale, $R(t)$ vs. t in Fig. 3(c), on a log–log scale. BCP melt follows the diffusive growth (i.e., $\phi \sim 1/3$) in an early spinodal time window up to $t_{sp} \simeq 8.0 \times 10^2$ such that $R(t_{sp}) \sim 4$ (equivalent to the average size of BCP sub-chains). The length scale then crosses over to saturation when the constraints imposed by the topological connection become evident. The saturating $R(t)$ marks the freezing microphase morphology for symmetric BCPs. A more precise way of computing the growth exponent is to plot ϕ_{eff} vs. $R(t)^{-1}$ from Eq. (11) and extract ϕ_{eff} from data extrapolation in the asymptotic limit. Such an exercise is shown in Fig. 3(d), which demonstrates that in the limit $R(t)^{-1} \to 0$, the growth exponent converges to $\phi_{eff} \to 0$.

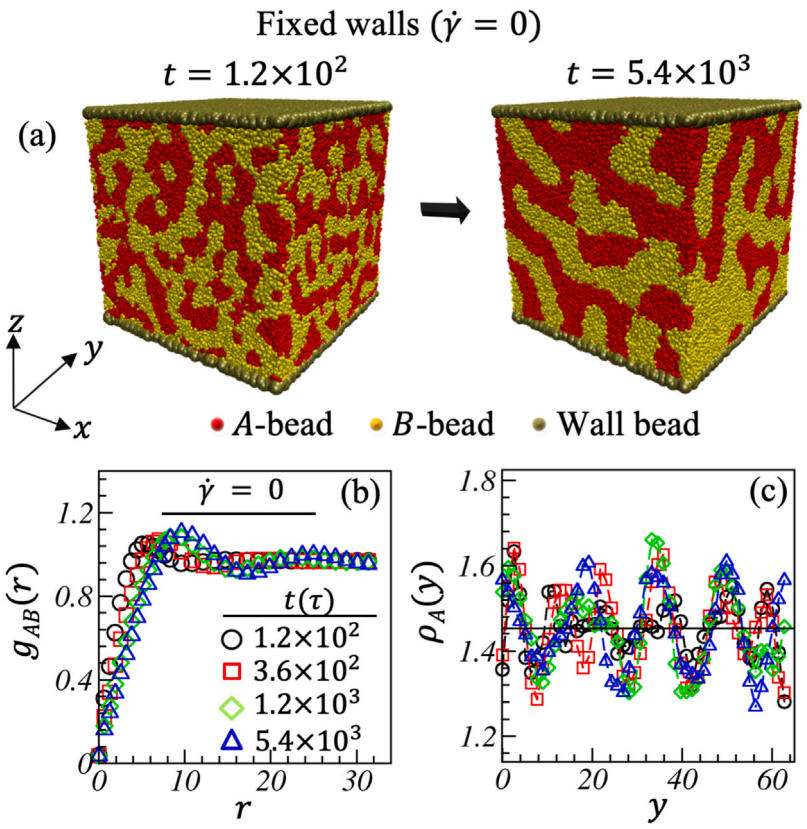

Fig. 2. The system is confined within fixed walls at the top and bottom, as indicated by the olive beads. (a) Evolution morphology of BCP melt at $t = 1.2 \times 10^2$ and $t = 5.4 \times 10^3$. (b) Comparison of the radial distribution function, $g_{AB}(r)$ versus r at different evolution times. (c) Average number density distribution, $\rho_A(y)$ of A-beads along y-direction for the same time steps as in (b).

3.2. Top wall moves

Let us return to the phase separation of BCP melt under the influence of shear arising due to moving walls. First, we focus on case 2, where the top wall moves in the positive x-direction, and the bottom wall is fixed. Any variation in the wall velocity can alter the shear rate; here, we choose three different shear rates, $\dot{\gamma} = 1.56 \times 10^{-3}$, 7.80×10^{-3}, and 1.56×10^{-2}, as mentioned earlier.

The evolution morphology for case 2 is displayed in Figs. S5. It is apparent that with the increase in $\dot{\gamma}$, domains of A and B sub-chains adjacent to the top wall appear to flow more along the shear direction. Recall that in case 1, the system could not develop lamellar morphology up to simulation time $t = 5.4 \times 10^3$. Herein, lamellar slabs appear earlier with increasing shear rates; the reason could be the flow and orientation of microdomains in the shear direction. Therefore, due to the competition of unidirectional shear and simultaneous microphase separation kinetics, BCP chains segregate perpendicular to the shear direction to form a more stable lamellar morphology than in any other adjustments. In other words, by adjusting normal to the shear direction, A and B domains try to overcome the effect of shear. Since only the top wall moves, the low shear rate ($\dot{\gamma} = 1.56 \times 10^{-3}$) primarily influences a small upper region of the simulation box. Thus, lamellar formation begins closer to the moving wall along the flow direction and perpendicular to the yz-plane. A few more layers in the simulation box are affected by the increase in shear rate, $\dot{\gamma} = 7.80 \times 10^{-3}$ and $\dot{\gamma} = 1.56 \times 10^{-2}$, and therefore, we get more ordered lamellar strips within the same time interval. The unidirectional shear enhances the tendency of lamellar pattern formation for a phase separating symmetric BCP melt.

To characterize the evolution morphology illustrated in Fig. S5, we plot $g_{AB}(r)$ vs. r in Fig. 4(a) at different time steps for $\dot{\gamma} = 7.80 \times 10^{-3}$. The black curve showed early time data when a few small microdomains evolved via spinodal decomposition. Thus, a single peak is observed at a shorter distance $r \simeq 5.0$. The main peak strength of $g_{AB}(r)$ increases with time and shows a relatively higher amplitude at $r \simeq 9.25$ at the late time (see the blue curve) than any other curves at earlier times. A secondary peak in $g_{AB}(r)$ is also clearly visible in the blue curve at a distance $r \simeq 24.0$. The main reason is the coarsening of lamellar morphology. Corresponding local number density profile, $\rho_A(y)$ is plotted against the y-direction in Fig. 4(b). A much lower density profile amplitude at early times verifies tiny microdomain formation (see the corresponding black and red curves). However, at late times, a more considerable amplitude and oscillatory behavior of $\rho_A(y)$ are observed due to larger and periodic domain coarsening.

Further, we compare $g_{AB}(r)$ vs. r in Fig. 4(c) to characterize the evolved morphologies at a late time for different shear rates. All the RDF curves present an excellent data overlap closer to the first peak; however, the main peak width slightly narrows as its position shifts to smaller $r \simeq 9.6$, 9.6, 9.25, and 9.0 with increasing shear rates. Subsequently, the secondary RDF peaks, which are developed due to the formation of periodic morphology, also shifted to its left at $r \simeq 25.0$, 24.32, 24.0, and 22.4 for $\dot{\gamma} = 0.0$, 1.56×10^{-3}, 7.80×10^{-3}, and 1.56×10^{-2}, respectively. Overall, these plots suggest increasing periodicity and the thinning of domain sizes with increasing shear rates. The much lower density profile ($\rho_A(y)$) amplitude at lower shear rates ($\dot{\gamma} = 0.0$, 1.56×10^{-3}), indicated by the back and red symbols in Fig. 4(d), imply that the periodic structures are not a fully developed lamellar—many short and randomly oriented domain stripes are still present in the system. In contrast, $\rho_A(y)$ gains significant height and periodicity at higher shear rates ($\dot{\gamma} = 7.80\times10^{-3}$, 1.56×10^{-2}), suggesting the evolution of appreciable lamellar morphology.

To see the effect of various shear rates on the dynamic scaling functions for case 2, we plot $C(r,t)$ vs. $r/R(t)$ in Fig. 5(a) and $S(k,t)$ vs. $kR(t)$ on a log–log scale in Fig. 5(b) for different shear rates at

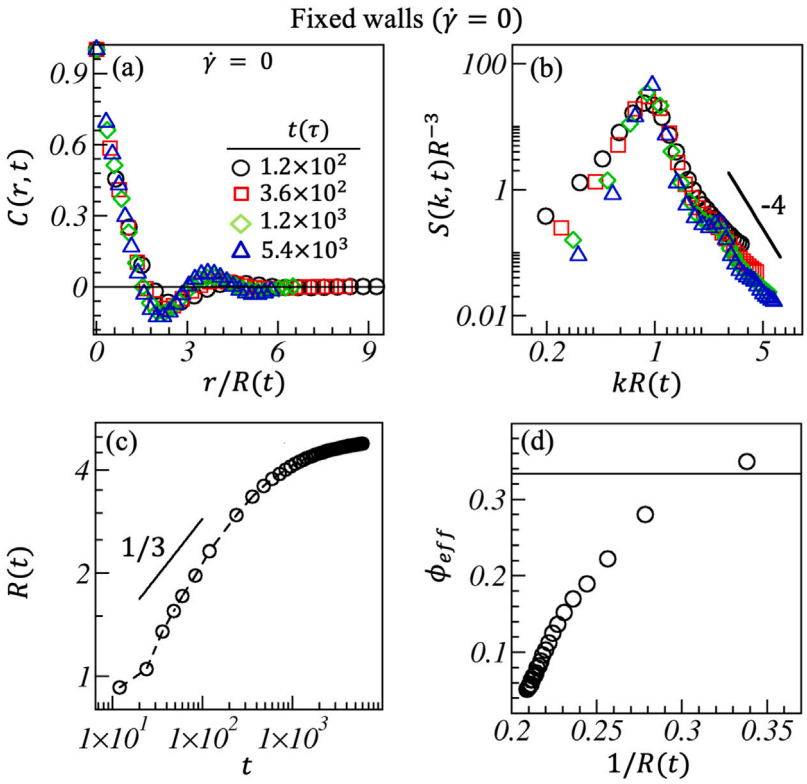

Fig. 3. Spherically averaged scaled functions and length scale for the evolution displayed in Fig. 2. (a) $C(r,t)$ versus $r/R(t)$ at different times for the fixed walls. The solid line guides the zero-crossing of $C(r,t)$. (b) $S(k,t)$ versus $kR(t)$ on a logarithmic scale for the same times as in (a). The solid line with slope −4 represents the Porod's law: $S(k,t) \sim k^{-4}$ at $k \to \infty$. (c) Characteristic length scale, $R(t)$ versus t for the same data sets as in (a) and (b). The solid line shows the diffusive growth law ($\phi \sim 1/3$) at early times, which gradually saturates later, illustrating usual microphase separation kinetics in BCP melt. (d) Presents effective growth exponent ϕ_{eff} versus $1/R(t)$. The solid line shows the reference value of $\phi_{eff} \sim 1/3$ for early diffusive growth.

$t = 5.4 \times 10^3$. The oscillatory $C(r,t)$ curves in Fig. 5(a) characterize the developing periodic morphology at late times; the appearance of the distinct shoulder at large $kR(t)$ for each curve in Fig. 5(b) verify the same. Notice the slight decrease in amplitude of oscillation in $C(r,t)$ and the broadening in $S(k,t)$s' main peak for $\dot{\gamma} \neq 0.0$. Since the first moment of $S(k,t)$ is inversely proportional to average domain size ($\langle k \rangle \sim R(t)^{-1}$) [12,13], the broadening of main $S(k,t)$ peak implies an increase in $\langle k \rangle$ with shear rate justifies shear-thinning at late times. Further, the shoulder in $S(k,t)$ shows up at smaller $kR(t) \simeq 2.67$ for $\dot{\gamma} = 0.0$ (black curve), whereas it appears at larger $kR(t) \simeq 3.06$ in the blue curve. Overall, these observations indicate the shear-thinning of morphologies. We notice that the black curves in Fig. 5(a-b) slightly deviate from the scaling. However, for $\dot{\gamma} \neq 0.0$, the scaling function data illustrates a good overlap; hence, they belong to the same universality class. A solid line with slope −4 in Fig. 5(b) shows that the scaled structure factor tail follows Porod's law for all cases.

Next, we compare the characteristic length scale, $R(t)$ vs. t on a logarithmic scale in Fig. 5(c) and the corresponding effective growth exponent in Fig. 5(d) for $\dot{\gamma} \neq 0.0$ values. The black curve for $\dot{\gamma} = 0.0$ is plotted for reference. Note that domain coarsening and their flow along the shear direction are two physical processes occurring simultaneously. The lower shear rate ($\dot{\gamma} = 1.56 \times 10^{-3}$, red curve) seems to complement the early-time domain growth ($R(t) \sim t^{1/3}$). Thus, we observe a larger average domain size up to the time, $t_{sp} \simeq 6.0 \times 10^2$, indicating lower shear-thinning than other higher shear rates. The topological constraint becomes apparent for $t > t_{sp}$. We notice a dip in the growth scale for a certain period ($6.0 \times 10^2 < t < 1.0 \times 10^3$) where A and B domains could be adjusted in a shear direction to minimize its effect. The length scale grows again and then crosses over to saturation, indicating the freezing in microdomain growth to a smaller length scale than in case 1 ($\dot{\gamma} = 0.0$), which marks the shear-thinning effect. The shear effect becomes prominent with increasing shear rate, which causes domain thinning from the early times. Thus, the overall growth rate decreases. Early-time growth exponent reduces from a pure diffusive growth $R(t) \sim t^{1/3}$, then crosses over to frozen microphase morphology at the late stages. The effective growth exponent, ϕ_{eff} vs. $1/R(t)$ curves in Fig. 5(d) again illustrate the same; $\phi_{eff} \to 0$ in the limit $1/R(t) \to 0$.

3.3. Both walls move in the same direction

Now, we turn our attention to case 3, where we shear the segregating BCP melt from both sides in the same direction and monitor its effect on the evolution morphology (displayed in Fig. S6) and the growth kinetics. The effect of shear on the morphology is getting more prominent from with increasing shear rates: $\dot{\gamma} = 7.80 \times 10^{-3}$ to 1.56×10^{-2}. The system begins to develop periodic structures from the top and bottom region of the simulation box, particularly closer to the walls where shear is more effective than in other areas. A more explicit lamellar morphology seemed to form herein than in case 2 at the same shear rates. The effect of lower shear rate, $\dot{\gamma} = 1.56 \times 10^{-3}$, on the evolving morphology emerges almost similar to what it was in case 2.

We plot $g_{AB}(r)$ for different shear rates in Fig. 6(a) at $t = 5.4 \times 10^3$. Similar to the previous cases, $g_{AB}(r)$ becomes more oscillatory with increasing shear rate, signifying increasing periodicity. The peak positions of $g_{AB}(r)$ move to their left with increasing shear rates (denoted by various symbols); the primary peak positions are at $r \simeq 9.6$, 9.5, 9.0, 9.0, and the secondary peaks are at $r \simeq 25.0$, 24.32, 23.04, 22.4, respectively. This indicates the thinning in average domain size with shear rates. The local density variation in Fig. 6(b) illustrates the equal distribution of $\rho_A(y)$ around its average value ($\rho_A = 1.453$). Their enhanced amplitude than previous cases signifies the formation of a

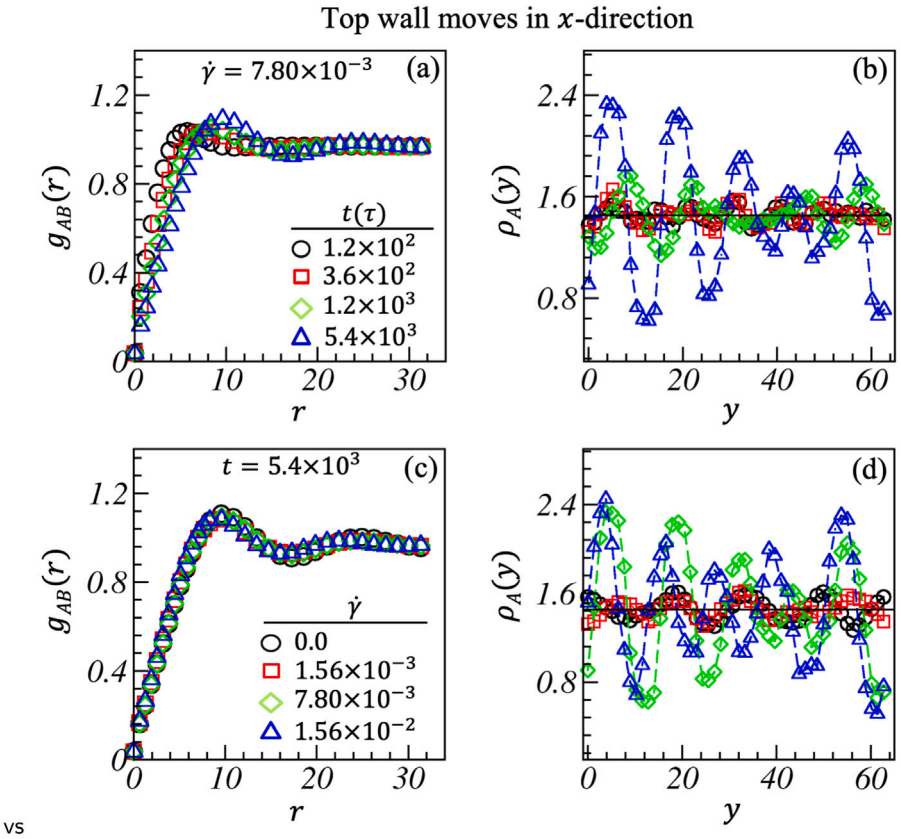

Fig. 4. Top wall is sheared with $\dot{\gamma} = 7.80 \times 10^{-3}$. (a) Plots for $g_{AB}(r)$ versus r at different times, indicated by various symbols. (b) $\rho(y)$ of A-beads along y-direction for the same time steps as in (a). (c) $g_{AB}(r)$ versus r for different top wall shear rates for case 2 at a fixed $t = 5.4 \times 10^3$. (d) $\rho(y)$ versus y for the same set of data as in (c).

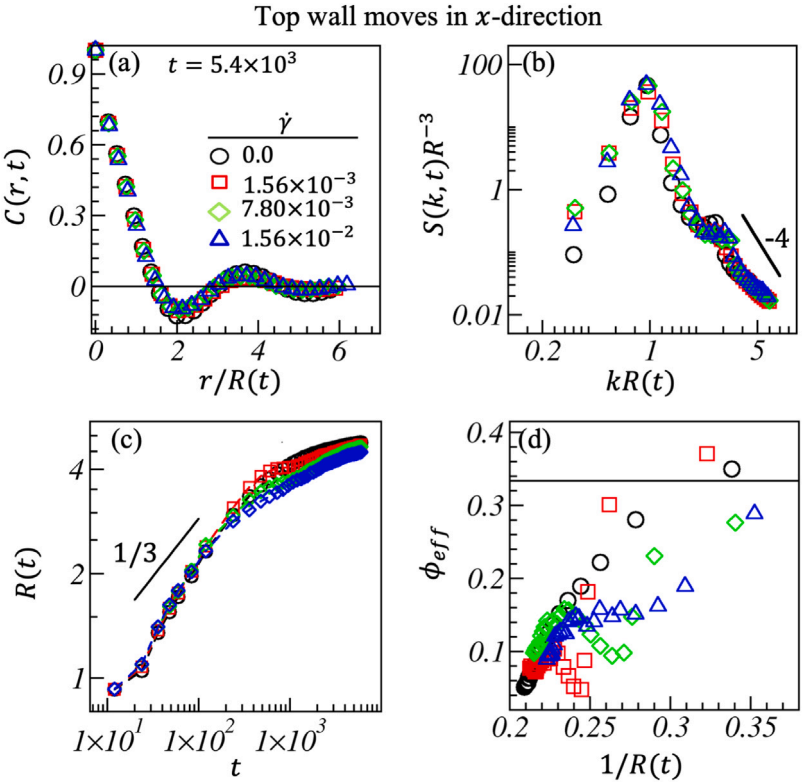

Fig. 5. Comparing scaling function, length scale, and effective growth exponent at $t = 5.4 \times 10^3$ for different shear rates for case 2 as indicated by the various symbol types. $C(r,t)$ versus $r/R(t)$ is displayed in (a), and corresponding $S(k,t)$ versus $kR(t)$ on a logarithmic scale in (b). (c) $R(t)$ versus t on a log–log scale at different shear rates for the evolution shown in Fig. (S5). The variation of growth exponent ϕ_{eff} as a function of $1/R(t)$ is in (d).

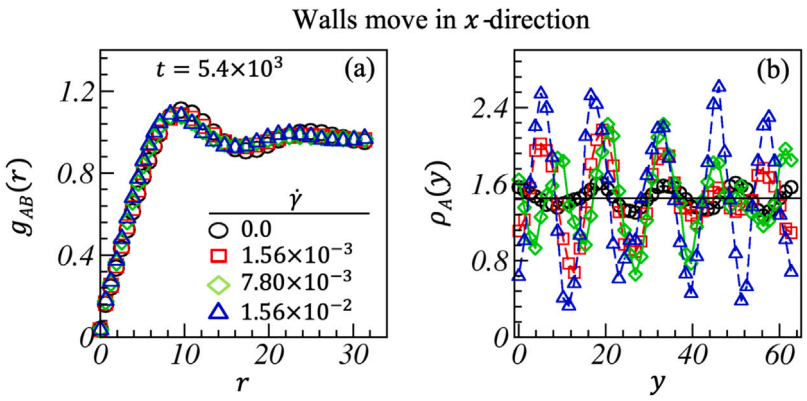

Fig. 6. Case 3: Both walls are moving with the same velocities in x-direction. (a) $g_{AB}(r)$ versus r, and (b) average number density profiles of A-type beads in y-direction at $t = 5.4 \times 10^3$ for different shear rates are presented with various open symbols; related morphologies are shown in Fig. (S6).

more well-formed lamellar morphology, perpendicular to the y-axis; see the green and blue curves at $\dot{\gamma} = 7.80 \times 10^{-3}$ and $\dot{\gamma} = 1.56 \times 10^{-2}$, respectively. Notice the red curve at $\dot{\gamma} = 1.56 \times 10^{-3}$, showing an apparent enhancement in $\rho_A(y)$ than in case 2; thus, we get a more ordered structure in case 3 than in case 2 with the same shear rates.

The late time dynamic scaling functions, $C(r,t)$ and $S(k,t)$ in Fig. 7(a) and (b) exhibit apparent deviation at $\dot{\gamma} = 1.56 \times 10^{-3}$ (red symbol) from the reference case (black curve) including the high shear cases, as displayed in green and blue marks. However, $C(r,t)$ and $S(k,t)$ curves at higher shear rates illustrate excellent data overlap, thus, exhibiting dynamical scaling. The structure factor shows Porod's tail ($S(k,t) \sim k^{-4}$) for all the shear rates for $kR(t) \to \infty$, indicating the sharp domain interface between A and B phases. The oscillation in the correlation function and the emergence of the shoulder at large $kR(t)$ in the structure factor represent the formation of the periodic structures. After the zero crossing, the smaller amplitude of oscillation in $C(r,t)$ and the broadening of the prominent peak in $S(k,t)$ with shear rates attribute to the shear-thinning of evolving morphologies.

Similar to case 2, the low shear rate complements the early time diffusive growth, and we observed a slightly larger average domain size up to $t_{sp} \simeq 6.0 \times 10^2$ (see the red curve in Fig. 7(c)). Then, a flattening of length scale data (*i.e.*, negligible domain growth) is observed up to $t \simeq 1.0 \times 10^3$ due to the competing process of shear and phase separation kinetics. The corresponding growth exponent (ϕ_{eff}) shows a significant dip (see the red curve in Fig. 7(d)). The BCP sub-chains are most likely arranged normal to the flow direction in this period to minimize the shear effect. Beyond this, domains begin to grow again with a lower growth rate due to shear-thinning than the reference case during the same period. The length scale tends to saturate at a slightly larger value than the reference case (see the red curves in Fig. 7(c–d)). The effect of higher shear rates is more prominent from the beginning; the growth exponent ($\phi_{eff} \simeq 0.2$) is smaller, as displayed by the green and blue curves in Fig. 7(c–d). The length scale tends to saturate to the lower values at late times, justifying the shear-thinning. Again, the shear-thinning is more prominent for the higher shear rate. Thus, in the limit of $R(t)^{-1} \to 0$, the effective growth exponent $\phi_{eff} \to 0$.

Recall that $C(r,t)$ and $S(k,t)$ denote the spherically averaged correlation function and the structure factor. The critical BCP melts evolve to form lamellar morphology in the asymptotic limit. Thus, it is essential to manifest the anisotropy developed in the system at late times. In this regard, Fig. 8(a) and (b) display the structure factor, $S(k_x, k_y, k_z)$ against the wave vector components, k_y (black curve) and k_z (red curve) for case 2 and case 3 at $\dot{\gamma} = 7.80 \times 10^{-3}$ for $t = 5.4 \times 10^3$. The black curve shows sharper and higher amplitude peaks in $S(k_x, k_y, k_z)$ along k_y (normal to the lamellar). The red curve shows a single low amplitude peak along k_z (parallel to the lamellar). Thus, both these curves justify the structural anisotropy in the system. The larger peak amplitude of the black curve for case 3 (Fig. 8(b)) explains a higher structure anisotropy than in case 2 (Fig. 8(a)). Notice the snapshots in Figs. S5-S6; they illustrate that lamellar slabs of each phase are coarsening nearly parallel to the xz-plane; thus, the variation of $S(k_x, k_y, k_z)$ along k_x and k_z is similar (comparison is not shown here due to brevity). However, excellent overlapping in green and blue curves in the insets of Fig. 8 affirms the symmetric arrangement of lamellar slabs in the yz-plane. The structure factor, $S(k_x, k_y, k_z)$ data is averaged over ten ensembles.

3.4. Both walls move in opposite directions

In case 4, wall motion generates equal and opposite shear in the x-direction. The evolution patterns in Fig. S7 suggest that the system forms lamellar morphology much earlier than in cases 1–3. The reason could be the opposite shear directions facilitate a more rapid readjustment of evolving microdomains; it is evident that well-developed lamellar patterns are formed for $\dot{\gamma} = 7.80 \times 10^{-3}$ and $\dot{\gamma} = 1.56 \times 10^{-2}$. However, the system comprises a few shorter patches of A and B domains, elongated in the x-direction, at $\dot{\gamma} = 1.56 \times 10^{-3}$.

As discussed earlier for other cases, $g_{AB}(r)$ vs. r in Fig. 9(a) shows a similar late time behavior for all shear rates. The peaks get more oscillatory and sharper with increasing shear rates due to the evolution of a more ordered and periodic lamellar morphology. A tiny shift in the first peak positions (at $r \simeq 9.5$, 9.0, 8.32) and a relatively larger change in secondary peak positions (at $r \simeq 24.96$, 22.40, 21.76) towards lower r indicates the shear-thinning of morphologies with shear rate. Fig. 9(b) illustrates that the amplitude of $\rho_A(y)$ vs. y increases with the shear rate. A significant increase in the amplitude of $\rho(y)$ and much sharper domain interfaces signify a well-separated morphology at high shear strength ($\dot{\gamma} = 1.56 \times 10^{-2}$), as displayed by the blue curve in Fig. 9(b). Nearly equal periodicity and amplitude of $\rho(y)$ profile along the y-direction manifests the formation of lamellar morphology normal to it at higher shear rates; see the green and blue curves in Fig. 9(b) at $\dot{\gamma} = 7.80 \times 10^{-3}$ and 1.56×10^{-2}.

The scaled $C(r,t)$ in Fig. 9(c) and the corresponding $S(k,t)$ in Fig. 9(d) demonstrate notable deviation from the dynamic scaling function in case 4. This is indifferent to case 2 and case 3, where we have observed the scaling in $C(r,t)$, at least up to the first zero crossing (at smaller r) and in $S(k,t)$ at larger $kR(t)$. Furthermore, $C(r,t)$ becomes more oscillatory at larger $r/R(t)$ with the increase in $\dot{\gamma}$. In $S(k,t)$, we observe prominent shoulders at larger $kR(t) \simeq 2.67$, 2.84, 2.86, and 2.93 for $\dot{\gamma} = 0.0$, 1.56×10^{-3}, 7.80×10^{-3}, and 1.56×10^{-2}, respectively. In addition, however, we notice the development of another shoulder at $kR(t) \simeq 4.68$ and 4.95 for $\dot{\gamma} = 7.80 \times 10^{-3}$ and 1.56×10^{-2}. These results verify the formation of a more periodic lamellar morphology with an increasing shear rate than for other cases. Moreover, a fully evolved periodic lamellar morphology was noted at $t = 5.4 \times 10^3$ for $\dot{\gamma} = 1.56 \times 10^{-2}$.

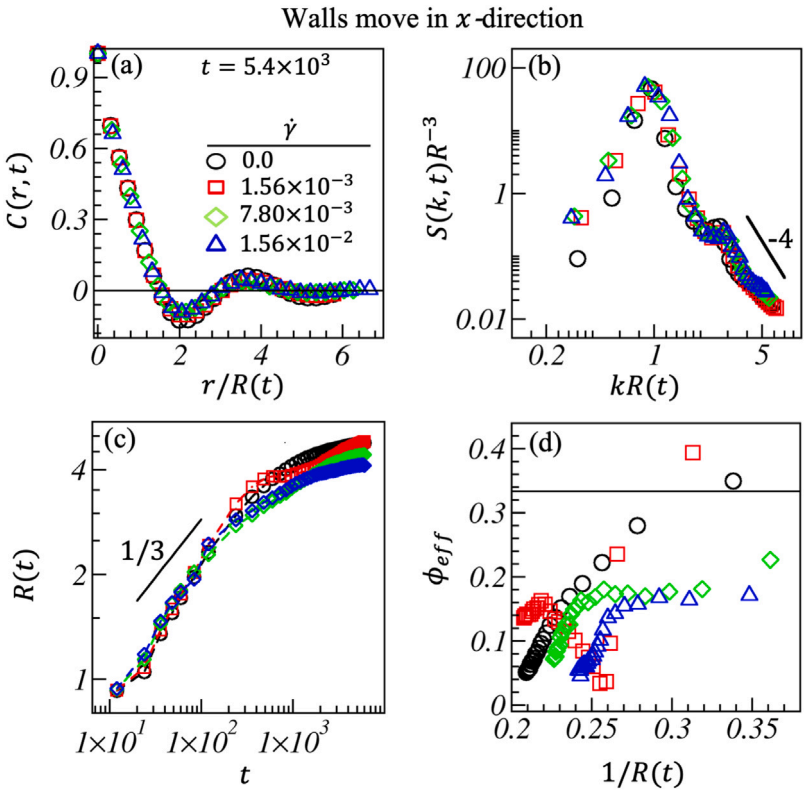

Fig. 7. (a) Comparison of $C(r,t)$ versus $r/R(t)$ at different shear rates for the morphologies illustrated in Fig. (S6). Corresponding $S(k,t)$ versus $kR(t)$ curves are in (b) on a logarithmic scale. The average domain size, $R(t)$ versus t, and related effective growth exponents ϕ_{eff} versus $1/R(t)$ are displayed in (c) and (d), respectively.

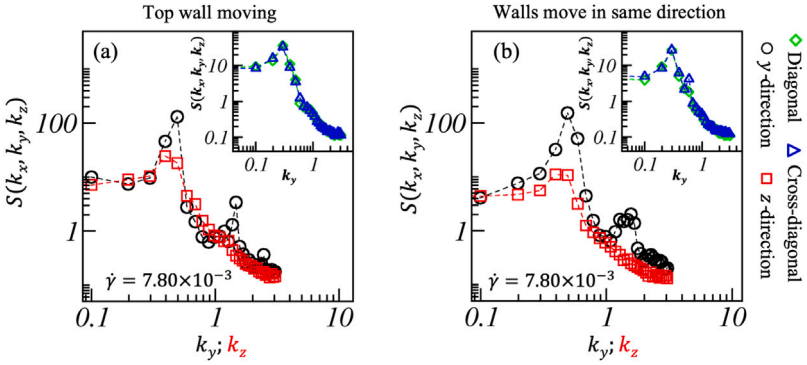

Fig. 8. Plot of $S(k_x,k_y,k_z)$ versus k_y (black curve) and k_z (red curve) at $\dot{\gamma} = 7.80\times10^{-3}$ to illustrate the structural anisotropy (a) for the top wall motion along x-direction, and (b) when both walls move in the same direction. The green and blue curves in the inset demonstrate $S(k_x,k_y,k_z)$ versus k_y along diagonal and cross-diagonal directions, respectively, in xz-plane.

The time evolution of characteristic length scale, $R(t)$ vs. t in Fig. 9(e), and the corresponding growth exponent, ϕ_{eff} vs. $1/R(t)$ in Fig. 9(f) demonstrate the coarsening kinetics under the influence of shear for case 4. The black curve represents the reference case, $\dot{\gamma} = 0.0$. Similar to the earlier cases, for $\dot{\gamma} = 1.56\times10^{-3}$, the length scale follows diffusive growth: $\phi \to 1/3$ up to $t_{sp} \simeq 6.0\times10^{2}$ (red curve); the growth rate is higher within this period for $\dot{\gamma} = 1.56\times10^{-3}$. Beyond this time, $R(t)$ deviates significantly. We find a gradual dip in length scale up to $t \simeq 1.4\times10^{3}$ (see the red curve in Fig. 9(e–f)); the reason could be the domination of the shear rate over the diffusive growth, which is already slowing down due to the topological constraint of BCP chains. Therefore, as noted earlier, BCP chains in microdomains are possibly rearranging perpendicular to the shear direction to reduce its effect may cause the dip during this period. The green and blue curves at $\dot{\gamma} = 7.80\times10^{-3}$ and 1.56×10^{-2} also illustrate a similar dip in growth at much earlier times. After the dip in growth, $R(t)$ begins to grow further, and in contrast to cases 1–3, it follows diffusive growth ($\phi \sim 1/3$) for all $\dot{\gamma} \neq 0.0$ for a longer period before saturating. The length scale fully saturates at a lower $R(t)$ for $\dot{\gamma} = 1.56\times10^{-2}$ (see the blue curves in Fig. 9(e–f)), which is evident from Fig. S7(c) exhibiting a well-formed lamellar morphology. However, the length scales for $\dot{\gamma} = 1.56\times10^{-3}$ and 7.80×10^{-3} seem to saturate at the black curve (reference case) at late times. The effective growth exponent in Fig. 9(f) demonstrates the saturation in length scale in the asymptotic limit. Overall, the effect of shear, rendered by the horizontal parallel walls moving in opposite directions, is significant in obtaining the typical lamellar morphology much earlier in the microphase separating critical BCP melt.

Note that the domain evolution kinetics of a critical BCP melt is a well-established microphase separation phenomenon. The growth law follows diffusive growth ($R(t) \sim t^{1/3}$) at early times, then a gradual slow down at intermediate times, and finally, at a late stage, it saturates to a frozen lamellar morphology [6]. For example, when no shear was

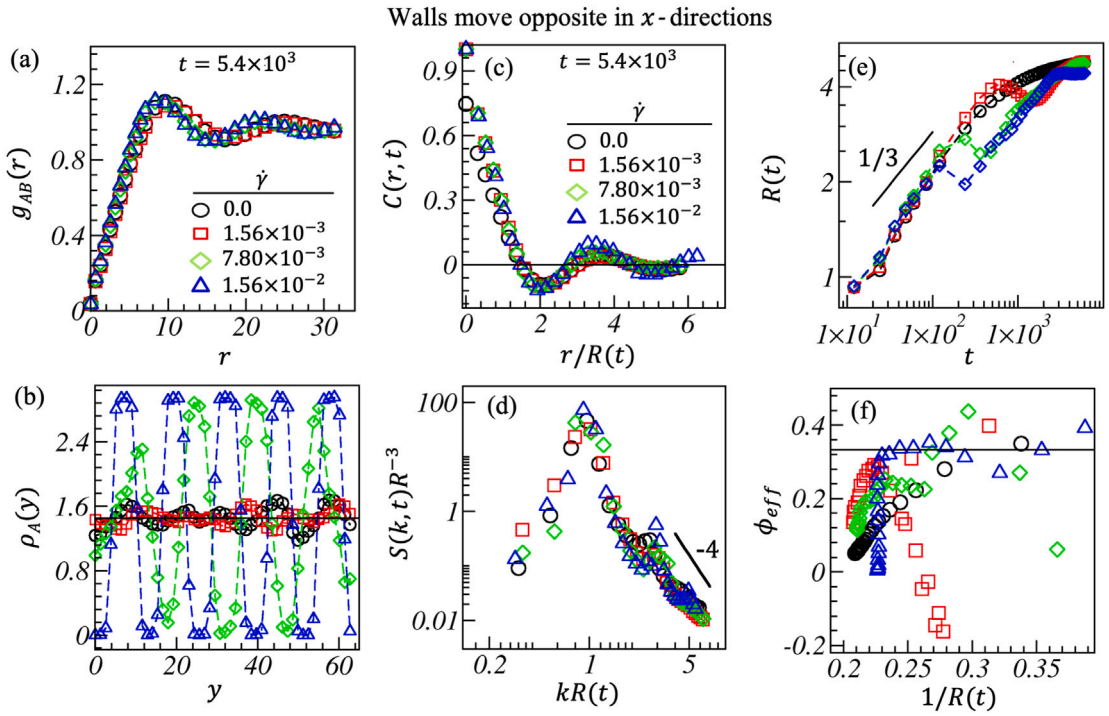

Fig. 9. Case 4: both walls are moving opposite in x-direction with the same velocities. Comparison of (a) $g_{AB}(r)$ versus r, (b) $\rho(y)$ versus y of A-type beads, (c) $C(r,t)$ versus $r/R(t)$, and (d) $S(k,t)$ versus $kR(t)$ at $t = 5.4 \times 10^3$ for different shear rates as shown with various open symbols. (e) The time dependence of average domain size $R(t)$ for the evolution is displayed in Fig. (S7). Corresponding effective growth exponents are plotted in (f).

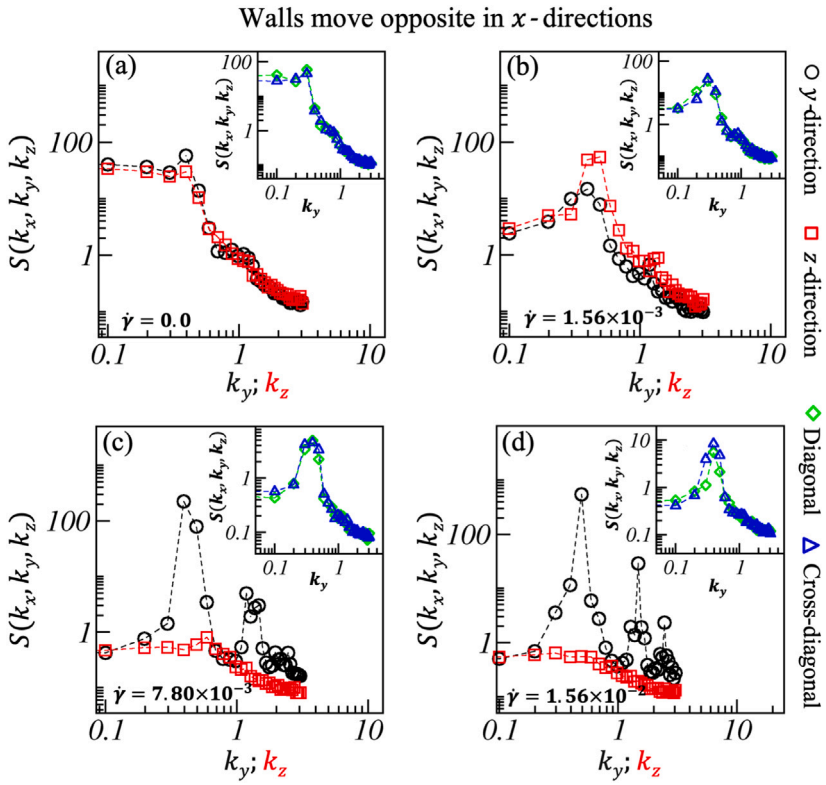

Fig. 10. The structure factor, $S(k_x, k_y, k_z)$ versus k_y (black curve) and k_z (red curve) for (a) $\dot{\gamma} = 0.0$, (b) $\dot{\gamma} = 1.56 \times 10^{-3}$, (c) $\dot{\gamma} = 7.80 \times 10^{-3}$, and (d) $\dot{\gamma} = 1.56 \times 10^{-2}$ to display the structural anisotropy in the system. The green and blue curves in the inset demonstrate $S(k_x, k_y, k_z)$ versus k_y along diagonal and cross-diagonal directions, respectively.

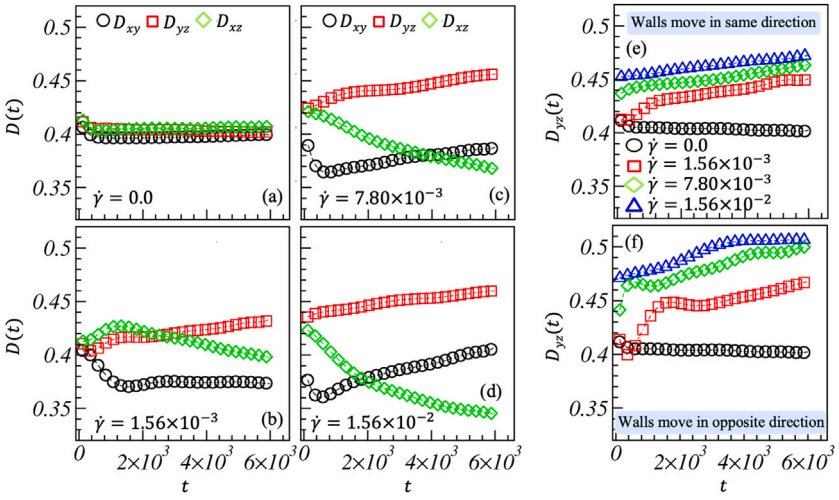

Fig. 11. Anisotropy parameters, D_{xy}, D_{yz}, and D_{xz} are plotted as a function of time for case 1 ($\dot{\gamma} = 0.0$) in (a) and for case 2 in (b-d) for different shear rates, $\dot{\gamma} = 1.56 \times 10^{-3}$, 7.80×10^{-3}, and 1.56×10^{-2}. Time variations of D_{yz} are compared in (e) and (f) for case 3 and case 4 at different shear rates depicted by various symbol types.

applied ($\dot{\gamma} = 0$), we had to wait for around $t \approx 2\times10^4$ to get the lamellar morphology for chain length $N_p = 32$ and the system size selected in our simulation. On the other hand, when the shear rate was high ($\dot{\gamma} = 1.56 \times 10^{-2}$) on both the walls and applied in opposite directions, the system evolved up to $t \approx 5 \times 10^3$ to form a lamellar morphology for the same system size. Therefore, we study the kinetics of all the cases within these two shear rates and time limits to emphasize the effect of shear on the evolved morphology via computing the growth laws and scaling functions as discussed above.

Recall that non-overlapping of the structure factor, $S(k_x, k_y, k_z)$ along different directions, k_x, k_y, and k_z represent the structural anisotropy in the system. Here, we discuss the anisotropy in the evolution morphology at a late time $t = 5.4\times10^3$ for $\dot{\gamma} = 0.0$, 1.56×10^{-3}, 7.80×10^{-3}, 1.56×10^{-2}, as displayed in Fig. 10(a–d). The black and red curves represent the variation of $S(k_x, k_y, k_z)$ vs. k_y (normal to the stripes) and k_z (along with the stripes). For $\dot{\gamma} = 0.0$, lamellar patterns are not fully developed in any particular direction. However, $S(k_x, k_y, k_z)$ data along k_y (black curve) shows a slightly larger peak and also a developing shoulder at larger k_y than in the red curve; this indicates that lamellar patterns may evolve normal to the y-direction at much longer times. Further, notice the stripes for $\dot{\gamma} = 1.56 \times 10^{-3}$ in Figs. S7(a), which are nearly parallel to the xy-plane (i.e., normal to the z-axis). Thus, we notice a moderately higher amplitude of structure factor peak at a smaller k_z (red curve) than in the black curve against k_y. However, an emerging shoulder is apparent in both curves for the large k_y and k_z.

As noted earlier from Figs. S7(b–c), more distinct lamellar stripes are formed at higher shear rates, i.e., at $\dot{\gamma} = 7.80\times10^{-3}$ and 1.56×10^{-2}, normal to the yz-plane along the x-direction. Therefore, we notice multiple sharp, high amplitude peaks in the structure factor along the y-direction (see the black curves in Fig. 10(c–d)); these peaks depict the periodic A and B-type stripes. In contrast, the structure factor peak seen in the red curve at lower shear rates diminishes at $\dot{\gamma} = 7.80\times10^{-3}$ and 1.56×10^{-2}. The reason is that the stripes get more and more parallel to the xz-plane with the increase in shear rate along the x-axis. Hence, these results verify the presence of anisotropy in the y-direction. Furthermore, the green and blue curves in the inset of Fig. 10(a–d) exhibit the variation in $S(k_x, k_y, k_z)$ along the diagonals in the yz-plane versus k_y. The excellent data overlap for all shear rates justifies the structural symmetry in the yz-plane along the diagonals. Also, notice the structure factor peaks shown by the green and blue curves; the main peaks get sharper and higher in amplitude with enhanced shear, indicating more ordered lamellar morphology. We average the $S(k_x, k_y, k_z)$ data over ten ensembles.

The time variation of the anisotropy parameter, $D(t)$, is plotted in Fig. 11 as denoted by various symbol types. Usually, due to structural constraints, phase separating BCP melts have inherent anisotropy. Therefore, for case 1, we have $D(t) \sim 0.4$ (see Fig. 11(a)), i.e., D_{xy}, D_{yz}, and D_{xz} values are approximately same in this case. Thus, at our simulation's time and length scale, the typical lamellar morphology for a symmetric BCP melt is not fully evolved yet for case 1 (reference case, see Figs. 2(a) and S4). For case 2, due to top wall shear in the x-direction, microdomains begin to reorient themselves in forming lamellar slabs parallel to the xz-plane (as in Fig. S5). As a result, $D(t)$ decreases in the xz-plane (green curve) and grows yz-planes (red curve) with time. Furthermore, we notice that the differences in $D(t)$ in different planes become more prominent at late times, particularly for higher shear rates. Thus, with the increase in shear rate, anisotropy in the x-direction (i.e., in the yz-plane) increases more due to more ordered evolved morphology and decreases in the xz-plane. At a low shear rate, $\dot{\gamma} = 1.56 \times 10^{-3}$, a decrease in D_{xy} (black curve in Fig. 11(b)) suggests that only small and local slabs of both the phases are developed in the xy-plane without any specific orientation. However, D_{xy} increases with higher shear rates. In Fig. 11(e) and (f), we compare the time variation of D_{yz} for case 3 and case 4 at different shear rates. In both cases, we observe that evolved morphologies are more anisotropic compared to case 2, as depicted in Fig. 11(b)–(d). Nevertheless, as discussed earlier, we find a clearer lamellar morphology for case 4; thus, the corresponding anisotropy parameter, D_{yz}, is also relatively higher than in cases 2 and 3. The corresponding evolution snapshots are presented in Figs. S5, S6 and S7, respectively.

4. Summary and conclusions

We utilize the DPD simulation technique to simulate the phase separation kinetics of the critical BCP bulk melts under three unidirectional shear conditions. The shear is applied by moving the parallel solid walls with a constant velocity in a particular direction only. The walls confine the cubic simulation box at the top and the bottom. The shear is allowed to affect the system in three ways: (i) only the top wall moves (case 2). (ii) Both walls move in the same direction (case 3). (iii) In the last case, both walls move in opposite directions (case 4). We discuss the effect of shear rendered in the system on evolution morphology, scaling functions, length scale, and growth law for different cases. Further, we compare the anisotropy induced in the system from the structure factor variation in different directions and justify it further by computing the anisotropy parameter. All the shear-influenced results are compared with no shear case, *i.e.*, when both the walls are fixed (case 1). Finally,

we present the variation in the averaged shear viscosity and velocity profiles for all the cases at different shear rates.

On the application of shear, microdomains start flowing along the shear direction. We notice that the lamellar formation always begins in the region close to the moving wall. One of our significant observations is that segregating BCP chains, regardless of chain size, begin to adjust perpendicular to the shear direction and along the wall plane to overcome its effect at moderate to high shear rates. This eventually leads to a periodic lamellar pattern much earlier than case 1 (without shear). However, a fully grown lamellar morphology is still not observed at the lower shear rate up to the simulation period used in this work; nonetheless, our results suggest they are more periodic than in case 1. The corresponding radial distribution function, the local density profile variation, and the comparison of structure factors in different directions perfectly characterized the morphology under various shear conditions. The late time correlation function and the structure factor offer a reasonably good scaling for all the shear rates in case 2 and case 3. However, in case 4, where the shear effect is more pronounced on the evolution morphology, the scaled correlation function and the structure factor deviated from the scaling for all the velocities. The oscillatory nature of the correlation function and the emerging shoulder at larger $kR(t)$ values in the structure factor further justify the segregating periodic morphology. Moreover, the broadening of the structure factor main peak at various shear rates signifies the shear-thinning of domain size in the asymptotic limit.

The competition between the microphase separation kinetics and the shearing through wall motion leads to some fascinating behavior of characteristic length scale. In particular, at lower shear rates, the flow of early small domains and individual BCP chains in the shear direction seems to complement the domain segregation. As a result, the average domain size becomes more prominent for all the cases at early times. The variation of average shear viscosity with shear rates justifies that at lower shear rates, shear viscosity is higher (i.e., low shear-thinning) than at moderate and high shear rates. Interestingly, near the length scale crossover to saturation for case 1, the length scale at the lower shear rates also slows significantly (the length scale became almost flat) for case 2 and case 3 within a specific time interval.

On the other hand, we observe negative growth for case 4 for a slightly larger period due to the shear effect dominating the diffusive growth during this time interval. As a result, the BCP chains are merely adjusting themselves to minimize the shear effect. Again, the length scale grows with time following the diffusive growth and then begins to saturate at a length scale reasonably lower or nearly equal to case 1 at late times for different cases. Furthermore, moderate and large shear rates dominate the diffusive growth from the beginning for almost all cases. Thus, the length scale growth rate, lower from early times, saturates to a lower length scale at late times, indicating the shear-thinning. Again, the variation of average shear viscosity with shear rates justifies the same.

Overall, this work illustrates the influence of unidirectional shear induced by moving amorphous solid walls on phase separation kinetics of the critical BCP bulk melts. Besides, this work can guide quickly producing bulk composite materials with diverse anisotropic morphology and various physical properties. Given the different scientific and technological importance of morphologies obtained from segregating BCP melts, these results will enable additional experimental and theoretical interest in this problem. Further, we hope this work will offer a broad framework to simulate the morphology growth in BCP melts and polymer blends under such an external response.

CRediT authorship contribution statement

Ashish Kumar Singh: Conceptualization, Methodology, Formal analysis, Investigation, Resources, Data curation, Writing – original draft, Visualization, Funding acquisition. **Awaneesh Singh:** Conceptualization, Validation, Formal analysis, Investigation, Writing – review and editing, Supervision, Funding acquisition.

Declaration of competing interest

The authors declare that they have no known competing financial interests or personal relationships that could have appeared to influence the work reported in this paper.

Data availability

Data will be made available on request

Acknowledgments

A.K.S. is grateful to the CSIR fellowship (File No: 09/1217(0074)/2019-EMR-I), New Delhi, for the financial support. A.S. acknowledges the financial support from Grant No. ECR/2017/002529 by the Science and Engineering Research Board, New Delhi, India.

Appendix A. Supplementary data

Supplementary material related to this article can be found online at https://doi.org/10.1016/j.commatsci.2023.112224.

References

[1] L. Leibler, Theory of microphase separation in block copolymers, Macromolecules 13 (6) (1980) 1602–1617, http://dx.doi.org/10.1021/ma60078a047.
[2] T. Hashimoto, M. Shibayama, H. Kawai, Domain-boundary structure of styrene-isoprene block copolymer films cast from solution. 4. Molecular-weight dependence of lamellar microdomains, Macromolecules 13 (5) (1980) 1237–1247, http://dx.doi.org/10.1021/ma60077a040.
[3] T. Ohta, K. Kawasaki, Equilibrium morphology of block copolymer melts, Macromolecules 19 (10) (1986) 2621–2632, http://dx.doi.org/10.1021/ma00164a028.
[4] F.S. Bates, G.H. Fredrickson, Block copolymer thermodynamics: theory and experiment, Annu. Rev. Phys. Chem. 41 (1) (1990) 525–557, http://dx.doi.org/10.1146/annurev.pc.41.100190.002521.
[5] I. Hamley, Ordering in thin films of block copolymers: Fundamentals to potential applications, Prog. Polym. Sci. 34 (11) (2009) 1161–1210, http://dx.doi.org/10.1016/j.progpolymsci.2009.06.003.
[6] A. Singh, R. Krishnan, S. Puri, Kinetics of microphase separation in block copolymers: A molecular-dynamics study, Europhys. Lett. 109 (2) (2015) 26006, http://dx.doi.org/10.1209/0295-5075/109/26006.
[7] A.A. Gavrilov, Y.V. Kudryavtsev, A.V. Chertovich, Phase diagrams of block copolymer melts by dissipative particle dynamics simulations, J. Chem. Phys. 139 (22) (2013) 224901, http://dx.doi.org/10.1063/1.4837215.
[8] M. Nebouy, J. Morthomas, C. Fusco, G.P. Baeza, L. Chazeau, Coarse-grained molecular dynamics modeling of segmented block copolymers: impact of the chain architecture on crystallization and morphology, Macromolecules 53 (10) (2020) 3847–3860, http://dx.doi.org/10.1021/acs.macromol.9b02549.
[9] M.C. Stuparu, A. Khan, C.J. Hawker, Phase separation of supramolecular and dynamic block copolymers, Polym. Chem. 3 (11) (2012) 3033–3044, http://dx.doi.org/10.1039/C2PY20368E.
[10] T. Beardsley, R. Spencer, M. Matsen, Computationally efficient field-theoretic simulations for block copolymer melts, Macromolecules 52 (22) (2019) 8840–8848, http://dx.doi.org/10.1021/acs.macromol.9b01904.
[11] K. Binder, Phase Transitions in Polymer Blends and Block Copolymer Melts: Some Recent Developments, Springer, 1994, pp. 181–299, http://dx.doi.org/10.1007/BFb0017984.
[12] A.J. Bray, Theory of phase-ordering kinetics, Adv. Phys. 51 (2) (2002) 481–587, http://dx.doi.org/10.1080/00018739400101505.
[13] S. Puri, V. Wadhawan (Eds.), Kinetics of Phase transitions, CRC Press, Boca Raton, Fla., 2009, http://dx.doi.org/10.1016/0167-5729(94)90009-4.
[14] A. Singh, S. Puri, C. Dasgupta, Kinetics of phase separation in polymer mixtures: A molecular dynamics study, J. Chem. Phys. 140 (24) (2014) 244906, http://dx.doi.org/10.1063/1.4884824.
[15] A. Singh, S. Puri, Phase separation in ternary fluid mixtures: a molecular dynamics study, Soft Matter 11 (11) (2015) 2213–2219, http://dx.doi.org/10.1039/C4SM02726D.
[16] A.K. Singh, A. Chauhan, S. Puri, A. Singh, Photo-induced bond breaking during phase separation kinetics of block copolymer melts: a dissipative particle dynamics study, Soft Matter 17 (7) (2021) 1802–1813, http://dx.doi.org/10.1039/D0SM01664K.
[17] A. Singh, A. Chakraborti, A. Singh, Role of a polymeric component in the phase separation of ternary fluid mixtures: a dissipative particle dynamics study, Soft Matter 14 (21) (2018) 4317–4326, http://dx.doi.org/10.1039/C8SM00625C.

[18] F. Liu, N. Goldenfeld, Dynamics of phase separation in block copolymer melts, Phys. Rev. A 39 (9) (1989) 4805, http://dx.doi.org/10.1103/PhysRevA.39.4805.
[19] N. Maurits, A. Zvelindovsky, G. Sevink, B. Van Vlimmeren, J. Fraaije, Hydrodynamic effects in three-dimensional microphase separation of block copolymers: Dynamic mean-field density functional approach, J. Chem. Phys. 108 (21) (1998) 9150–9154, http://dx.doi.org/10.1063/1.476362.
[20] R.D. Groot, T.J. Madden, D.J. Tildesley, On the role of hydrodynamic interactions in block copolymer microphase separation, J. Chem. Phys. 110 (19) (1999) 9739–9749, http://dx.doi.org/10.1063/1.478939.
[21] R.D. Groot, T.J. Madden, Dynamic simulation of diblock copolymer microphase separation, J. Chem. Phys. 108 (20) (1998) 8713–8724, http://dx.doi.org/10.1063/1.476300.
[22] Y. Shiwa, Hydrodynamic interactions in microphase separation of block copolymer films: Stability and spirals, Phys. Rev. E 61 (3) (2000) 2924, http://dx.doi.org/10.1103/PhysRevE.61.2924.
[23] A. Xu, G. Gonnella, A. Lamura, G. Amati, F. Massaioli, Scaling and hydrodynamic effects in lamellar ordering, Europhys. Lett. 71 (4) (2005) 651, http://dx.doi.org/10.1209/epl/i2005-10130-3.
[24] H. Feng, X. Lu, W. Wang, N.-G. Kang, J.W. Mays, Block copolymers: Synthesis, self-assembly, and applications, Polymers 9 (10) (2017) 494, http://dx.doi.org/10.3390/polym9100494.
[25] M.P. Stoykovich, P.F. Nealey, Block copolymers and conventional lithography, Mater. Today 9 (9) (2006) 20–29, http://dx.doi.org/10.1016/S1369-7021(06)71619-4.
[26] C. Harrison, J.A. Dagata, D.H. Adamson, et al., Lithography with self-assembled block copolymer microdomains, Wiley Chichester, 2004, p. 295, http://dx.doi.org/10.1002/0470093943.
[27] A. Rosler, G.W. Vandermeulen, H.-A. Klok, Advanced drug delivery devices via self-assembly of amphiphilic block copolymers, Adv. Drug Deliv. Rev. 64 (2012) 270–279, http://dx.doi.org/10.1016/S0169-409X(01)00222-8.
[28] R.K. O'Reilly, C.J. Hawker, K.L. Wooley, Cross-linked block copolymer micelles: functional nanostructures of great potential and versatility, Chem. Soc. Rev. 35 (11) (2006) 1068–1083, http://dx.doi.org/10.1039/B514858H.
[29] T.-Y. Ma, L. Liu, Z.-Y. Yuan, Direct synthesis of ordered mesoporous carbons, Chem. Soc. Rev. 42 (9) (2013) 3977–4003, http://dx.doi.org/10.1039/C2CS35301F.
[30] B. Fraser, C. Denniston, M.H. Muser, On the orientation of lamellar block copolymer phases under shear, J. Chem. Phys. 124 (10) (2006) 104902, http://dx.doi.org/10.1063/1.2177245.
[31] S.R. Ahmed, S.B. Ogale, P. Kofinas, Magnetic properties and morphology of block copolymer templated ferrimagnetic CoFe/sub 2/O/sub 4/nanoparticles, IEEE Trans. Magn. 39 (5) (2003) 2198–2200, http://dx.doi.org/10.1109/TMAG.2003.817074.
[32] T. Thurn-Albrecht, J. Schotter, G.A. Kastle, N. Emley, T. Shibauchi, L. Krusin-Elbaum, K. Guarini, C. Black, M. Tuominen, T. Russell, Ultrahigh-density nanowire arrays grown in self-assembled diblock copolymer templates, Science 290 (5499) (2000) 2126–2129, http://dx.doi.org/10.1126/science.290.5499.2126.
[33] I.W. Hamley, Structure and flow behaviour of block copolymers, J. Condens. Matter Phys. 13 (33) (2001) R643, http://dx.doi.org/10.1088/0953-8984/13/33/201.
[34] T. Morkved, M. Lu, A. Urbas, E. Ehrichs, H. Jaeger, P. Mansky, T. Russell, Local control of microdomain orientation in diblock copolymer thin films with electric fields, Science 273 (5277) (1996) 931–933, http://dx.doi.org/10.1126/science.273.5277.931.
[35] S. Ouk Kim, H.H. Solak, M.P. Stoykovich, N.J. Ferrier, J.J. De Pablo, P.F. Nealey, Epitaxial self-assembly of block copolymers on lithographically defined nanopatterned substrates, Nature 424 (6947) (2003) 411–414, http://dx.doi.org/10.1038/nature01775.
[36] G. Arya, J. Rottler, A.Z. Panagiotopoulos, D.J. Srolovitz, P.M. Chaikin, Shear ordering in thin films of spherical block copolymer, Langmuir 21 (24) (2005) 11518–11527, http://dx.doi.org/10.1021/la0516476.
[37] K. Almdal, K.A. Koppi, F.S. Bates, Dynamically sheared body-centered-cubic ordered diblock copolymer melt, Macromolecules 26 (15) (1993) 4058–4060, http://dx.doi.org/10.1021/ma00067a053.
[38] G.A. McConnell, M.Y. Lin, A.P. Gast, Long range order in polymeric micelles under steady shear, Macromolecules 28 (20) (1995) 6754–6764, http://dx.doi.org/10.1021/ma00124a009.
[39] D.B. Scott, A.J. Waddon, Y.G. Lin, F.E. Karasz, H.H. Winter, Shear-induced orientation transitions in triblock copolymer styrene-butadiene-styrene with cylindrical domain morphology, Macromolecules 25 (16) (1992) 4175–4181, http://dx.doi.org/10.1021/ma00042a019.
[40] K.A. Koppi, M. Tirrell, F.S. Bates, Shear-induced isotropic-to-lamellar transition, PRL 70 (10) (1993) 1449, http://dx.doi.org/10.1103/PhysRevLett.70.1449.
[41] K.I. Winey, S.S. Patel, R.G. Larson, H. Watanabe, Interdependence of shear deformations and block copolymer morphology, Macromolecules 26 (10) (1993) 2542–2549, http://dx.doi.org/10.1021/ma00062a024.
[42] Z.-R. Chen, A. Issaian, J. Kornfield, S. Smith, J. Grothaus, M. Satkowski, Dynamics of shear-induced alignment of a lamellar diblock: a rheo-optical, electron microscopy, and X-ray scattering study, Macromolecules 30 (23) (1997) 7096–7114, http://dx.doi.org/10.1021/ma9706743.
[43] D.E. Angelescu, J.H. Waller, D.H. Adamson, P. Deshpande, S.Y. Chou, R.A. Register, P.M. Chaikin, Macroscopic orientation of block copolymer cylinders in single-layer films by shearing, Adv. Mater. 16 (19) (2004) 1736–1740, http://dx.doi.org/10.1002/adma.200400643.
[44] D.E. Angelescu, J.H. Waller, R.A. Register, P.M. Chaikin, Shear-induced alignment in thin films of spherical nanodomains, Adv. Mater. 17 (15) (2005) 1878–1881, http://dx.doi.org/10.1002/adma.200401994.
[45] A. Nikoubashman, R.A. Register, A.Z. Panagiotopoulos, Simulations of shear-induced morphological transitions in block copolymers, Soft Matter 9 (42) (2013) 9960–9971, http://dx.doi.org/10.1039/C3SM51759D.
[46] B.L. Peters, A. Ramirez-Hernandez, D.Q. Pike, M. Muller, J.J. de Pablo, Nonequilibrium simulations of lamellae forming block copolymers under steady shear: A comparison of dissipative particle dynamics and Brownian dynamics, Macromolecules 45 (19) (2012) 8109–8116, http://dx.doi.org/10.1021/ma301541f.
[47] C. Stegelmeier, A. Exner, S. Hauschild, V. Filiz, J. Perlich, S.V. Roth, V. Abetz, S. Förster, Evaporation-induced block copolymer self-assembly into membranes studied by in situ synchrotron SAXS, Macromolecules 48 (5) (2015) 1524–1530, http://dx.doi.org/10.1021/ma502375h.
[48] M. D'Haese, P. Van Puyvelde, F. Langouche, Effect of particles on the flow-induced crystallization of polypropylene at processing speeds, Macromolecules 43 (6) (2010) 2933–2941, http://dx.doi.org/10.1021/ma9027933.
[49] V. Preziosi, A. Perazzo, G. Tomaiuolo, V. Pipich, D. Danino, L. Paduano, S. Guido, Flow-induced nanostructuring of gelled emulsions, Soft Matter 13 (2017) 5696–5703, http://dx.doi.org/10.1039/C7SM00646B.
[50] C. Caiazza, V. Preziosi, G. Tomaiuolo, D. O'Sullivan, V. Guida, S. Guido, Flow-induced concentration gradients in shear-banding of branched wormlike micellar solutions, J. Colloid Interface Sci. 534 (2019) 695–703, http://dx.doi.org/10.1016/j.jcis.2018.09.060.
[51] K. Sankhala, D.C.F. Wieland, J. Koll, M. Radjabian, C. Abetz, V. Abetz, Self-assembly of block copolymers during hollow fiber spinning: an in situ small-angle X-ray scattering study, Nanoscale 11 (2019) 7634–7647, http://dx.doi.org/10.1039/C8NR06892E.
[52] R.D. Groot, P.B. Warren, Dissipative particle dynamics: Bridging the gap between atomistic and mesoscopic simulation, J. Chem. Phys. 107 (11) (1997) 4423–4435, http://dx.doi.org/10.1063/1.474784.
[53] P. Espanol, P. Warren, Statistical mechanics of dissipative particle dynamics, Europhys. Lett. 30 (4) (1995) 191, http://dx.doi.org/10.1209/0295-5075/30/4/001.
[54] P. Espanol, P.B. Warren, Perspective: Dissipative particle dynamics, J. Chem. Phys. 146 (15) (2017) 150901, http://dx.doi.org/10.1063/1.4979514.
[55] R.D. Groot, A local galilean invariant thermostat, J. Chem. Theory Comput. 2 (3) (2006) 568–574, http://dx.doi.org/10.1021/ct050269e.
[56] P. Nikunen, M. Karttunen, I. Vattulainen, How would you integrate the equations of motion in dissipative particle dynamics simulations? Comput. Phys. Comm. 153 (3) (2003) 407–423, http://dx.doi.org/10.1016/S0010-4655(03)00202-9.
[57] P. Nikunen, I. Vattulainen, M. Karttunen, Reptational dynamics in dissipative particle dynamics simulations of polymer melts, Phys. Rev. E 75 (3) (2007) 036713, http://dx.doi.org/10.1103/PhysRevE.75.036713.
[58] S. Plimpton, Fast parallel algorithms for short-range molecular dynamics, J. Comput. Phys. 117 (1) (1995) 1–19, http://dx.doi.org/10.1006/jcph.1995.1039.
[59] V. Symeonidis, G.E. Karniadakis, B. Caswell, Schmidt number effects in dissipative particle dynamics simulation of polymers, J. Chem. Phys. 125 (18) (2006) 184902, http://dx.doi.org/10.1063/1.2360274.
[60] C. Junghans, M. Praprotnik, K. Kremer, Transport properties controlled by a thermostat: An extended dissipative particle dynamics thermostat, Soft Matter 4 (1) (2008) 156–161, http://dx.doi.org/10.1039/B713568H.
[61] B. Nikoobakht, M.A. El-Sayed, Preparation and growth mechanism of gold nanorods (NRs) using seed-mediated growth method, Chem. Mater. 15 (10) (2003) 1957–1962, http://dx.doi.org/10.1021/cm020732l.
[62] H.-P. Hsu, K. Kremer, Static and dynamic properties of large polymer melts in equilibrium, J. Chem. Phys. 144 (15) (2016) 154907, http://dx.doi.org/10.1063/1.4946033.
[63] T.W. Sirk, Y.R. Slizoberg, J.K. Brennan, M. Lisal, J.W. Andzelm, An enhanced entangled polymer model for dissipative particle dynamics, J. Chem. Phys. 136 (13) (2012) 134903, http://dx.doi.org/10.1063/1.3698476.
[64] A. Esteves, K. Lyakhova, L. Van Der Ven, R. Van Benthem, G. De With, Surface segregation of low surface energy polymeric dangling chains in a cross-linked polymer network investigated by a combined experimental–simulation approach, Macromolecules 46 (5) (2013) 1993–2002, http://dx.doi.org/10.1021/ma302236w.
[65] Y. Liu, O. Kuksenok, X. He, M. Aizenberg, J. Aizenberg, A.C. Balazs, Harnessing cooperative interactions between thermoresponsive aptamers and gels to trap and release nanoparticles, ACS Appl. Mater. Interfaces 8 (44) (2016) 30475–30483, http://dx.doi.org/10.1021/acsami.6b06575.
[66] Y. Liu, G.T. McFarlin IV, X. Yong, O. Kuksenok, A.C. Balazs, Designing composite coatings that provide a dual defense against fouling, Langmuir 31 (27) (2015) 7524–7532, http://dx.doi.org/10.1021/acs.langmuir.5b00888.
[67] M. Sega, M. Sbragaglia, L. Biferale, S. Succi, Regularization of the slip length divergence in water nanoflows by inhomogeneities at the angstrom scale, Soft Matter 9 (35) (2013) 8526–8531, http://dx.doi.org/10.1039/C3SM51508G.

[68] M. Moseler, U. Landman, Formation, stability, and breakup of nanojets, Science 289 (5482) (2000) 1165–1169, http://dx.doi.org/10.1126/science.289.5482.1165.
[69] F. Muller-Plathe, Reversing the perturbation in nonequilibrium molecular dynamics: An easy way to calculate the shear viscosity of fluids, Phys. Rev. E 59 (5) (1999) 4894, http://dx.doi.org/10.1103/PhysRevE.59.4894.
[70] M.S. Kelkar, J.L. Rafferty, E.J. Maginn, J.I. Siepmann, Prediction of viscosities and vapor–liquid equilibria for five polyhydric alcohols by molecular simulation, Fluid Phase Equilib. 260 (2) (2007) 218–231, http://dx.doi.org/10.1016/j.fluid.2007.06.033.
[71] A. Onuki, M. Doi, Flow birefringence and dichroism of polymers. I. General theory and application to the dilute case, J. Chem. Phys. 85 (2) (1986) 1190–1197, http://dx.doi.org/10.1063/1.451315.
[72] G. Zhang, Z. Qin, Y. Qian, J. Zhu, Microstructural evolution and kinetics of phase separation in binary polymer blends under electric fields, Comput. Mater. Sci. 213 (2022) 111659, http://dx.doi.org/10.1016/j.commatsci.2022.111659.
[73] Y. Oono, S. Puri, Computationally efficient modeling of ordering of quenched phases, PRL 58 (8) (1987) 836, http://dx.doi.org/10.1103/PhysRevLett.58.836.
[74] A. Singh, A. Mukherjee, H. Vermeulen, G. Barkema, S. Puri, Control of structure formation in phase-separating systems, J. Chem. Phys. 134 (4) (2011) 044910, http://dx.doi.org/10.1063/1.3530784.
[75] Y. Oono, S. Puri, Study of phase-separation dynamics by use of cell dynamical systems. i. modeling, Phys. Rev. A 38 (1) (1988) 434, http://dx.doi.org/10.1103/PhysRevA.38.434.
[76] S. Majumder, S.K. Das, Temperature and composition dependence of kinetics of phase separation in solid binary mixtures, Phys. Chem. Chem. Phys. 15 (31) (2013) 13209–13218, http://dx.doi.org/10.1039/C3CP50612F.
[77] A. Singh, S. Puri, H. Mishra, Domain growth in chiral phase transitions, Nuclear Phys. A 864 (1) (2011) 176–202, http://dx.doi.org/10.1016/j.nuclphysa.2011.06.023.
[78] B. Konig, O.J. Ronsin, J. Harting, Two-dimensional cahn–hilliard simulations for coarsening kinetics of spinodal decomposition in binary mixtures, Phys. Chem. Chem. Phys. 23 (43) (2021) 24823–24833, http://dx.doi.org/10.1039/D1CP03229A.
[79] D.A. Huse, C.L. Henley, Pinning and roughening of domain walls in ising systems due to random impurities, PRL 54 (25) (1985) 2708, http://dx.doi.org/10.1103/PhysRevLett.54.2708.
[80] A. Statt, M.P. Howard, A.Z. Panagiotopoulos, Unexpected secondary flows in reverse nonequilibrium shear flow simulations, Phys. Rev. Fluids 4 (4) (2019) 043905, http://dx.doi.org/10.1103/PhysRevFluids.4.043905.
[81] W. Jiang, J. Huang, Y. Wang, M. Laradji, Hydrodynamic interaction in polymer solutions simulated with dissipative particle dynamics, J. Chem. Phys. 126 (4) (2007) 044901, http://dx.doi.org/10.1063/1.2428307.
[82] P.-G. De Gennes, Scaling Concepts in Polymer Physics, Cornell University Press, 1979.
[83] D. Jaramillo-Cano, M. Camargo, C.N. Likos, I.C. Garlea, Dynamical properties of concentrated suspensions of block copolymer stars in shear flow, Macromolecules 53 (22) (2020) 10015–10027, http://dx.doi.org/10.1021/acs.macromol.0c01365.
[84] G. Porod, Small Angle X-Ray Scattering, Academic Press, New York, 1982, http://dx.doi.org/10.1002/actp.1985.010360520.